*J. Fluid Mech.* (1999), *vol.* 398, *pp.* 109–153. Printed in the United Kingdom



# Simulation of boundary layer transition induced by periodically passing wakes

By XIAOHUA WU[1], ROBERT G. JACOBS[1], JULIAN C. R. HUNT[2] AND PAUL A. DURBIN[1]

[1]Center for Integrated Turbulence Simulations, Flow Physics and Computation Division, Department of Mechanical Engineering, Stanford University, Building 500, Stanford, CA 94305-3030, USA
e-mail: wu@transition.stanford.edu; rjacobs@vk.stanford.edu; durbin@vk.stanford.edu

[2]Department of Applied Mathematics and Theoretical Physics, University of Cambridge, Cambridge CB3 9EW, UK
e-mail: jrh2@hermes.cam.ac.uk

(Received 9 September 1998 and in revised form 1 June 1999)

The interaction between an initially laminar boundary layer developing spatially on a flat plate and wakes traversing the inlet periodically has been simulated numerically. The three-dimensional, time-dependent Navier–Stokes equations were solved with $5.24 \times 10^7$ grid points using a message passing interface on a scalable parallel computer. The flow bears a close resemblance to the transitional boundary layer on turbomachinery blades and was designed following, in outline, the experiments by Liu & Rodi (1991). The momentum thickness Reynolds number evolves from $Re_\theta = 80$ to 1120. Mean and second-order statistics downstream of $Re_\theta = 800$ are of canonical flat-plate turbulent boundary layers and are in good agreement with Spalart (1988).

In many important aspects the mechanism leading to the inception of turbulence is in agreement with previous fundamental studies on boundary layer bypass transition, as summarized in Alfredsson & Matsubara (1996). Inlet wake disturbances inside the boundary layer evolve rapidly into longitudinal puffs during an initial receptivity phase. In the absence of strong forcing from free-stream vortices, these structures exhibit streamwise elongation with gradual decay in amplitude. Selective intensification of the puffs occurs when certain types of turbulent eddies from the free-stream wake interact with the boundary layer flow through a localized instability. Breakdown of the puffs into young turbulent spots is preceded by a wavy motion in the velocity field in the outer part of the boundary layer.

Properties and streamwise evolution of the turbulent spots following breakdown, as well as the process of completion of transition to turbulence, are in agreement with previous engineering turbomachinery flow studies. The overall geometrical characteristics of the matured turbulent spot are in good agreement with those observed in the experiments of Zhong *et al.* (1998). When breakdown occurs in the outer layer, where local convection speed is large, as in the present case, the spots broaden downstream, having the vague appearance of an arrowhead pointing upstream.

The flow has also been studied statistically. Phase-averaged velocity fields and skin-friction coefficients in the transitional region show similar features to previous cascade experiments. Selected results from additional thought experiments and simulations are also presented to illustrate the effects of streamwise pressure gradient and free-stream turbulence.

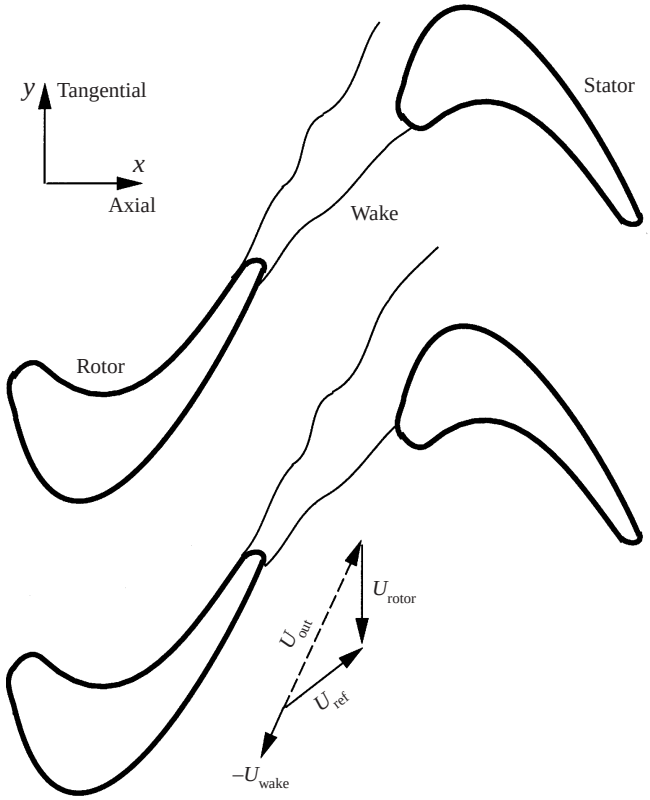


FIGURE 1. Sketch of rotor–stator wake interaction; $U_{rotor}$: rotor velocity in the stator reference frame; $U_{out}$: rotor exit flow velocity in the rotor reference frame; $U_{ref}$: stator inflow velocity in the stator reference frame.

## 1. Introduction

Upstream and downstream blade interactions in the passages of multi-stage axial turbomachines result in a complex and inherently unsteady flow field. Specifically, the boundary layer over a blade surface is subjected to a substantial degree of unsteadiness that stems from impinging wakes of the upstream stator or rotor (figure 1). The full turbomachinery configuration includes other disturbances, but wake impingement is the dominant effect at subsonic Mach numbers (Korakianitis 1993; Hodson 1998). The pronounced effect of upstream wakes arises primarily because large regions of laminar and transitional flows exist on the suction surface of embedded stages. The impinging vortical, turbulent wake markedly alters the path to transition.

There are a number of mechanisms for the way in which eddies and organized disturbances interact with an adjacent boundary layer that is initially laminar. These have been identified in recent research, but their combined effect in any given flow is difficult to understand and to predict. The first question is to define which of the entrainment or external mechanisms are relevant: do perturbations in the boundary layer emanate from an upstream edge or inlet and grow within the boundary layer, or are internal disturbances induced directly by external disturbances that move above the layer? This is the general question of receptivity paths for bypass transition (Goldstein & Wundrow 1998; Leib, Wundrow & Goldstein 1999; Jacobs & Durbin 1998). In the case of incident turbulent wakes, large external downdrafts or gusts

may be deflected by the vorticity of the layer through the sheltering mechanism of Hunt & Durbin (1999), or they may penetrate the boundary layer to produce locally amplifying turbulent spots.

The second question concerns how the fluctuations are transformed within the boundary layer and how the layer itself is changed. Instabilities may be triggered at subcritical Reynolds numbers (Corral & Jimenez 1994) through the action of finite-amplitude disturbances. Only very low level forcing produces transition via Tollmein–Schlichting waves. Moderate or high level forcing leads to transition via formation of localized turbulent spots without Tollmein–Schlichting precursors (Mayle 1991). Once induced, these disturbances grow within the boundary layer, although their development may be influenced by modulation of the boundary layer by the free-stream distortion.

The specific receptivity path and internal growth mechanics depend on the particular flow configuration (Hunt & Durbin 1999). However, general questions can be asked within the scope of transition induced by localized, convected external disturbances that either enter the flow domain abruptly or are rapidly distorted at a leading edge.

There are several mechanisms operative in passing wake-induced bypass transition. The mean wakes distort boundary layer profiles and the wakes are distorted by the wall: does this significantly alter the receptivity and transition processes? Fluctuations are created as the turbulent wake enters the flow domain: are these the origin of turbulent spots, or do their long-wavelength components just modulate the downstream transition mechanism? The convected wakes carry free-stream turbulence over the boundary layer: are these free-stream eddies the primary source of transitional spots? The present simulations address these questions.

This paper describes a spatially developing, three-dimensional, time-accurate DNS of boundary layer transition induced by periodically passing wakes (figure 2). The incident wakes are generated as self-similar free shear flows, but the manner of their introduction into the flow domain requires an inevitable distortion near the wall. However, that distortion is well defined and reproducible.

### 1.1. *The connection with some fundamental work on bypass transition*

There is now a sizable body of literature from fundamental studies of boundary layer bypass transition due to moderate-amplitude free-stream turbulence. It was realized by us, only retrospectively, that the problem at hand shares important features with some of the previous experimental, theoretical and numerical studies. These common characteristics are related to the physical mechanisms leading to the inception of turbulent spots, their growth through the transition region, and the manner in which they maintain the downstream turbulent region.

Experiments by Alfredsson & Matsubara (1996) in a laminar boundary layer subjected to 1.5% and 6% free-stream turbulence showed that during the initial receptivity and evolution phase, free-stream turbulence induces longitudinal streaks with a fairly periodic, spanwise regularity inside the boundary layer. These structures grow downstream both in length and amplitude. Breakdown to turbulent spots was observed to occur in the regions where smoke visualization exhibited intensive streaks. The breakdown of streaks often occurs after a wavy motion of the streaks, although spots occur locally and abruptly, not via amplification of the wavy motion to the point of breakdown. The turbulent spots grow in number and size downstream, until the boundary layer becomes fully turbulent. Similar streaky structures inside laminar and transitional boundary layers were observed by Grek, Kozlov & Ramazanov (1985) and termed puffs; streaks were also found in transitional channel flow (Klingmann

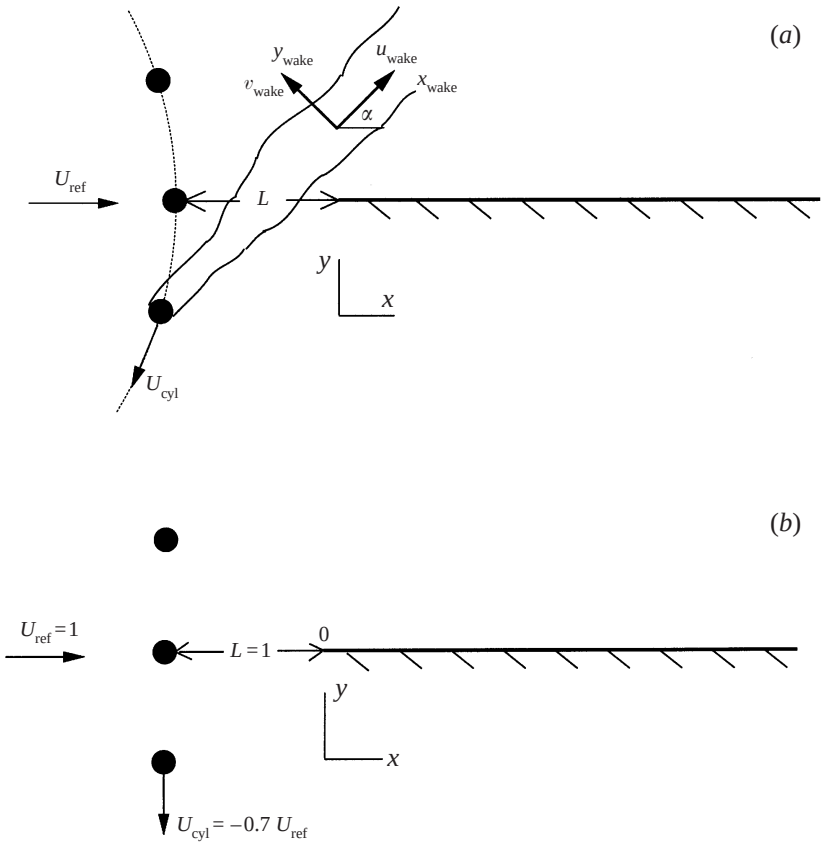


FIGURE 2. (*a*) Layout in the experiments of Liu & Rodi (1991); (*b*) layout in the present numerical simulation; the computational domain is defined as $0.1 \leqslant x/L \leqslant 3.5$, $0 \leqslant y/L \leqslant 0.8$, $0 \leqslant z/L \leqslant 0.2$.

1992; Henningson, Lundbladh & Johansson 1993) and in flows experiencing oblique transition (Berlin, Lundbladh & Henningson 1994).

Previous research on bypass transition induced by free-stream turbulence left open to interpretation the issue of whether intensification and ultimate destruction of the streaky structures arises from boundary layer internal dynamics, or from forcing by free-stream eddies. Such ambiguity is primarily due to experimental difficulties in following the details of the generation and growth of disturbances because of their randomness in space and time.

Figure 3(*a–c*) illustrates three scenarios observed in the present investigation (see § 4). In the most interesting case of those drawn in figure 3, inlet wake disturbances rapidly evolve into puffs similar to those found in Westin *et al.* (1994) and Alfredsson & Matsubara (1996) and turbulent spots appear downstream. More usually, the puffs decay as in figure 3(*b*), at least below the critical Reynolds number $Re_\theta = 200$. Turbulent eddies inside the passing free-stream wake impinge on the boundary layer and sometimes interact with its outer part, such as to subject the flow to a rapidly growing instability (§ 4). This involves an intensification of the near-wall streaky structures, and eventually the breakdown into young turbulent spots. Figures 3(*d*) and 3(*e*) depict two other scenarios in which the flow is subjected to very strong or extremely weak disturbances from the passing wake. Observations concerning the

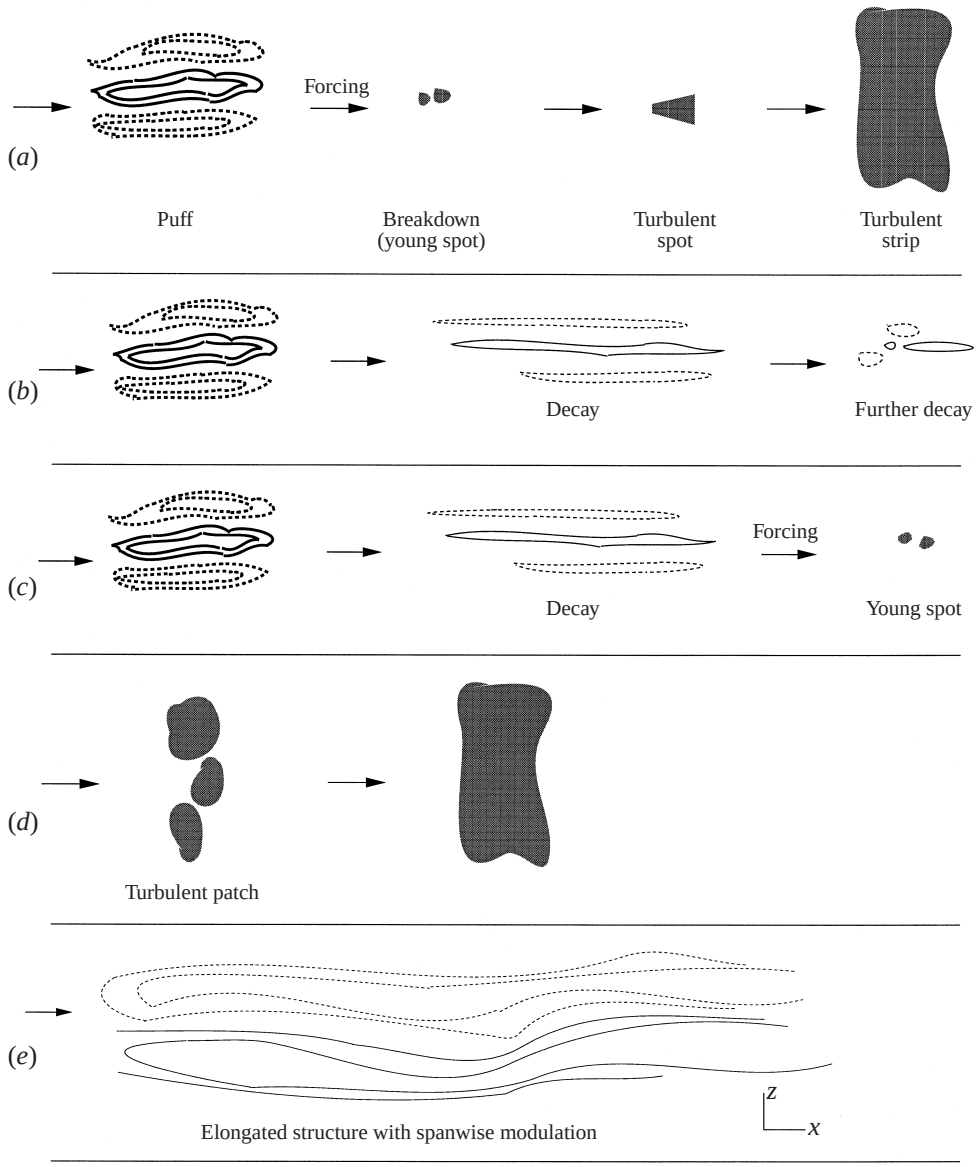


FIGURE 3. Several possibilities for the downstream propagation of certain types of inlet disturbances. The sketches represent $u'$ in an $(x, z)$-plane very close to the wall: (*a*) intermediate-strength disturbance and strong forcing; (*b*) intermediate-strength disturbance and weak forcing; (*c*) intermediate-strength disturbance with downstream strong forcing; (*d*) strong disturbance; (*e*) very weak disturbance.

last two instances have been made in the present study through additional numerical simulations and 'thought' experiments (see § 7).

### 1.2. *The connection with some engineering turbomachinery research*

Experiments on wake-induced periodic unsteady transition in turbomachinery blade rows were reported by Dring *et al.* (1982), Dong & Cumpsty (1990), Addison & Hodson (1990), Mayle & Dullenkopf (1991), and Halstead *et al.* (1997) (see also

the reviews by Mayle 1991 and Walker 1993). Halstead *et al.* (1996) reported measurements in compressors and low-pressure turbines. Their experiments showed that transition in unsteady, turbomachine boundary layers develops along two different, but coupled, paths. These consist of a wake-induced strip under the convecting wake trajectory, and a path between wakes that is caused by other disturbances. Along both paths the boundary layer goes from laminar to transitional to turbulent, with large regions of laminar and transitional flow. The switch from the non-wake path to the wake-induced strip was found to occur in a small fraction of a blade passing period. Halstead *et al.* noted that assumptions of predominantly turbulent boundary layers on multi-stage turbomachine blading are incorrect.

Although turbine and compressor experiments have indicated that the effects of wake passing can be substantial and have provided useful guidelines for further research, the technical complexities involved in obtaining detailed quantitative data from rotating turbine/compressor stages make it difficult to isolate physical mechanisms. Realizing such complexities, a number of investigators have considered simpler geometries. In the simplest of these (Pfeil, Herbst & Schroder 1983; Liu & Rodi 1991; Orth 1993; Zhong *et al.* 1998) the unsteady blade row interaction was simulated by sweeping a row of wake-generating cylinders past a flat plate (figure 2). Liu & Rodi (1991) obtained time- and phase-averaged mean and fluctuating streamwise velocity profiles for four different wake passing frequencies. In their experiments, the Reynolds number was fairly low so that the boundary layer remained laminar over the full plate length when no disturbing wakes were present. They found that the wake-produced turbulent strips grew together and caused the boundary layer to become fully turbulent. The streamwise location of the merger moved upstream with increasing wake passing frequency.

Using experimental data gathered from a similar flow configuration, Orth (1993) concluded that in turbomachinery flows periodically disturbed by passing wakes, the disturbance enters the boundary layer very early on, and convects within it before leading to transition. Periodic fluctuation in the velocity profile, as opposed to stochastic fluctuation, does not have a major influence on the transition. This is consistent with the present study. Orth (1993) also suggested that the location where transition takes place is only dependent on inlet turbulence intensity: the passing wake exerts no effect on the process. Our study shows that this needs qualification. Inception of turbulent spots in wake-induced transitional flows is intimately linked with turbulent eddies of the travelling free-stream wake. One additional pleasant connection of the present study with turbomachinery research concerns the recent liquid crystal visualization experiments of Zhong *et al.* (1998) and Kittichaikarn *et al.* (1999). This work was communicated to us by Prof. Hodson. Our turbulent spots, as well as their embryo precursors, resemble those observed by Zhong *et al.* (1998) and Kittichaikarn *et al.* (1999) to a remarkable degree (see § 3 and § 4).

## 2. Mathematical and numerical considerations

### 2.1. *Problem definition*

Consider the evolution of an incompressible flow over a smooth flat plate with upstream wakes passing periodically (figure 2*b*). The origin of the coordinate system is at the leading edge of the plate. The wakes are assumed to be generated by imaginary circular cylinders positioned in the plane $x = -L$ and moving in the $y$-direction at $U_{\mathrm{cyl}}$, which can be either positive or negative, corresponding to inlet wakes

traversing away from, or towards, the flat plate. The velocity of the flow upstream of the cylinder is $U_{\text{ref}}$. The cylinders are equally spaced so that they cut through the $y = 0$ plane at a specified passing period $\mathscr{T}$. The characteristic velocity scale is $U_{\text{ref}}$, the characteristic length scale is $L$, the Reynolds number is then $Re = U_{\text{ref}}L/\nu$ where $\nu$ is the kinematic viscosity of the fluid. Throughout this study $Re = 1.5 \times 10^5$, as in Liu & Rodi (1991). The mean flow properties of the wake are determined by free-stream velocity, cylinder velocity and cylinder diameter.

The computational domain for the DNS is defined as $0.1 \leqslant x/L \leqslant 3.5$, $0 \leqslant y/L \leqslant 0.8$, and $0 \leqslant z/L \leqslant 0.2$. The inlet momentum thickness Reynolds number is $Re_\theta = 80$ in all the simulations. Unless otherwise noted, all velocities are normalized by the reference velocity $U_{\text{ref}}$ and all lengths by the characteristic length scale $L$.

### 2.2. *Governing equations and notation*

Mass and momentum conservation is enforced for flow over the flat plate by solving the full time-dependent, mass-conservation and Navier–Stokes equations in Cartesian coordinates,

$$\operatorname{div} \boldsymbol{u} = 0, \tag{1}$$

$$\frac{\partial \boldsymbol{u}}{\partial t} + \operatorname{div}(\boldsymbol{u}\boldsymbol{u}) = -\frac{1}{\rho}\operatorname{grad} p + \operatorname{div}\left\{\frac{1}{Re}\left[\operatorname{grad}\boldsymbol{u} + (\operatorname{grad}\boldsymbol{u})^{\mathscr{S}}\right]\right\}, \tag{2}$$

where $\boldsymbol{u}$ is the velocity vector with Cartesian components $(u, v, w)$ or $u_i, i = 1, 2, 3$. Superscript $\mathscr{S}$ denotes transpose. The equations are in non-dimensional form.

In this paper, time-averaging is represented by $\overline{\cdot}$. Averaging at a particular phase, $t^m_{n_\mathscr{T}} = m\mathscr{T} + n_\mathscr{T}\mathscr{T}$, is denoted by $\langle\cdot\rangle$, where $m$ is any integer and $0 \leqslant n_\mathscr{T} \leqslant 1$ is the fraction of the wake passing period. For example, the phase-averaged mean velocity components are evaluated as

$$\langle u_i\rangle(t_{n_\mathscr{T}}) = \frac{1}{M}\sum_{m=1}^{M} u_i(t^m_{n_\mathscr{T}}), \tag{3}$$

where $M$ is the total number of periods within which phase averaging is performed. Averaging over the homogeneous spanwise $z$-direction is implied in both time-averaging and phase-averaging. Time-averaged and phase-averaged mean velocities are related via $\overline{u}_i = \overline{\langle u_i\rangle}$. Thus the instantaneous velocity can be decomposed as

$$u_i = \langle u_i\rangle(t_{n_\mathscr{T}}) + u_i'(t_{n_\mathscr{T}}) = \overline{u}_i + \tilde{u}_i(t_{n_\mathscr{T}}) + u_i'(t_{n_\mathscr{T}}), \tag{4}$$

where $\tilde{u}_i(t_{n_\mathscr{T}}) = \langle u_i\rangle(t_{n_\mathscr{T}}) - \overline{u}_i$ is the periodic velocity fluctuation with respect to the time-averaged mean, and $u_i'(t_{n_\mathscr{T}})$ is the true stochastic turbulence fluctuation. Consequently, the time-averaged Reynolds stresses $\overline{\langle u_i'u_j'\rangle}$ can be calculated as

$$\overline{\langle u_i'u_j'\rangle} = \int_0^1 \left\langle \left[u_i - \langle u_i\rangle(t_{n_\mathscr{T}})\right]\left[u_j - \langle u_j\rangle(t_{n_\mathscr{T}})\right]\right\rangle \mathrm{d}n_\mathscr{T}. \tag{5}$$

### 2.3. *Inflow and other boundary conditions*

For all the simulations described in this paper, the height of the computational domain $0.8L$ is approximately $200\delta$ at the inlet $x = 0.1L$, $20\delta$ in the middle of the plate $x = 1.75L$, and $11\delta$ at the exit $x = 3.5L$. $\delta(x)$ is the 99% boundary layer thickness. The width of the computational domain $0.2L$ is equivalent to $40\delta$ at the inlet, $5\delta$ in the middle of the plate and $3\delta$ at the exit.

Depending upon the passing frequency $1/\mathscr{T}$, at any given instant either one single wake or multiple wakes can be found on the inflow plane. A wake will be found on the computational inflow plane if its centreline is located within the range from $y = -b\cos\alpha$ to $y = 0.8L + b\cos\alpha$, where $b$ is wake half-width and $\alpha = \tan^{-1}U_{\mathrm{cyl}}/U_{\mathrm{ref}}$ is the wake inclination angle (figure 2). The total number of such wakes at any time is

$$\mathscr{N} = \mathrm{CEILING}\left(\frac{0.8L + 2b\cos\alpha}{|U_{\mathrm{cyl}}|\mathscr{T}}\right), \tag{6}$$

where the function CEILING returns the smallest integer greater than or equal to its real argument.

Consider $U_{\mathrm{cyl}} < 0$. On the inflow plane at the beginning of each wake passing period ($t^m_{n_{\mathscr{T}}} = 0$), let the origin of the uppermost wake-coordinate system ($x_{\mathrm{wake},1} = 0$, $y_{\mathrm{wake},1} = 0$) start to move downwards from $y = 0.8L + b\cos\alpha$. This indicates that at $t^m_{n_{\mathscr{T}}} = 0$ the wake starts to enter the top boundary of the inflow plane. At any subsequent time $0 < t^m_{n_{\mathscr{T}}} < \mathscr{T}$ the origin of the wake-coordinate system will be at $y_{\mathrm{centreline}} = 0.8L + b\cos\alpha + t^m_{n_{\mathscr{T}}}U_{\mathrm{cyl}}$. Each point on the inflow plane then has an effective coordinate with respect to the origin of the wake-coordinate system, which is $y_{\mathrm{eff,wake}}(y) = (y - y_{\mathrm{centreline}})/\cos\alpha$.

For $U_{\mathrm{cyl}} > 0$, the origin of the wake-coordinate system starts to move upwards from $y = -b\cos\alpha$. This indicates that at $t^m_{n_{\mathscr{T}}} = 0$ the wake starts to enter the lower boundary of the inflow plane. At any subsequent time the origin of its wake-coordinate system will be at $y_{\mathrm{centreline}} = -b\cos\alpha + t^m_{n_{\mathscr{T}}}U_{\mathrm{cyl}}$. Each point on the inflow plane then has an effective $y_{\mathrm{wake}}$-coordinate with respect to the origin of the wake-coordinate system, which is $y_{\mathrm{eff,wake}}(y) = (y - y_{\mathrm{centreline}})/\cos\alpha$.

At the inflow station of the computational domain $x = 0.1L$, the velocity components were prescribed as

$$\left.\begin{aligned} u &= u_{\mathrm{blasius}} + u_{\mathrm{blasius}}\left(\cos\alpha\sum_{q=1}^{\mathscr{N}} u_{\mathrm{eff,wake},q} - \sin\alpha\sum_{q=1}^{\mathscr{N}} v_{\mathrm{eff,wake},q}\right),\\ v &= v_{\mathrm{blasius}} + u_{\mathrm{blasius}}\left(\sin\alpha\sum_{q=1}^{\mathscr{N}} u_{\mathrm{eff,wake},q} + \cos\alpha\sum_{q=1}^{\mathscr{N}} v_{\mathrm{eff,wake},q}\right),\\ w &= \sum_{q=1}^{\mathscr{N}} w_{\mathrm{eff,wake},q}, \end{aligned}\right\} \tag{7}$$

where subscript blasius denotes the steady Blasius profile. The subscript eff, wake, $q$ represents the effective instantaneous velocity components in the $q$th wake-coordinate system. The velocities ($u_{\mathrm{eff,wake},q}, v_{\mathrm{eff,wake},q}, w_{\mathrm{eff,wake},q}$) are the same as the wake velocities ($u_{\mathrm{wake}}, v_{\mathrm{wake}}, w_{\mathrm{wake}}$) illustrated in figure 2 if $|y_{\mathrm{eff,wake},q}| \leqslant b$, and zero otherwise. The wake velocities were multiplied by $u_{\mathrm{blasius}}$ so they would satisfy no slip where the wake intersects the plate. As the wake enters the computational domain, a more realistic profile develops rapidly. Distortion of the velocities at the inlet results in a localized streamwise pressure gradient. The effect of such a pressure gradient on transition and boundary layer development will be studied in § 7 through numerical experiments.

In general, the mean velocity profile in wakes at a large distance from a solid body is independent of the shape of the body, except for a scale factor (Schlichting 1979). Liu & Rodi (1991) also pointed out that near the leading edge of the plate the cylinder wake is self-similar, and has also lost its shedding characteristics. Raj & Lakshminarayna (1973) demonstrated that the wake behind an airfoil trailing edge is

similar to that of a two-dimensional cylinder wake. Invoking self-similarity allows the wake introduced at the inlet to be obtained more simply than by actually computing a real cylinder wake.

The turbulent wake velocities ($u_{\text{wake}}$, $v_{\text{wake}}$, $w_{\text{wake}}$) appearing in (7) were generated from a separate precomputation of a temporally decaying, self-similar plane wake, following the work of Moser, Rogers & Ewing (1998) and Ghosal & Rogers (1997) . In a temporally decaying wake, the flow is statistically homogeneous in the streamwise and spanwise directions, and inhomogeneous in the cross-stream direction. The initial conditions for the temporally decaying plane wake simulation were generated from a turbulent channel flow simulation at Reynolds number 3300 based on the centreline mean velocity and channel half-height. The procedure involved taking two realizations of half-channel flow and 'fusing' them together. Physically this corresponds to a situation in which two half-channel flows exist on either side of a rigid plate and the plate is instantaneously removed. This simulation was performed on a grid size of (65, 128, 128) using an LES code (Wu & Squires 1997). The grid sizes used by Ghosal & Rogers (1997) and Moser *et al.* (1998) were (65, 48, 16) and (512, 195, 128), respectively.

Mean flow and turbulence statistics of the simulated plane wake are presented in figure 4. All velocities in the figure are normalized by the maximum mean velocity deficit $\overline{u}_{\text{wake, max}}$; lengths are normalized by the wake half-width $b$. Following Ghosal & Rogers (1997) , the half-width $b$ is defined as the distance between the two points at which the mean velocity deficit is $50\%\overline{u}_{\text{wake, max}}$. This is slightly larger than the distance between the wake centreline and the first point with effectively zero mean velocity deficit. Figure 4($a$) shows that mean velocity profiles obtained at the three different instants (indicated in the caption by their descending maximum velocity deficits) collapse. These mean profiles are also in excellent agreement with experimental measurements and the data correlation of Schlichting (1979), i.e. $\overline{u}_{\text{wake}}/\overline{u}_{\text{wake, max}} = [1 - (y_{\text{wake}}/1.1338b)^{1.5}]^2$. This demonstrates that the simulated wake has reached a self-similar state and that the mean flow has lost its memory of the initial condition. At these and subsequent instants, the product of the wake width and maximum deficit remains constant.

Figure 4($b, c$) show the r.m.s. turbulence intensities for the decaying plane wake at the same three instants. Turbulent shear stress profiles are given in figure 4($d$). The turbulence intensities obtained by Moser *et al.* (1998) and Ghosal & Rogers (1997) have two distinct features: double peaks occur in the streamwise component, and the wall-normal component is slightly higher than the spanwise component. In addition, the results of Ghosal & Rogers show that unlike the mean flow and the anti-symmetrical Reynolds shear stress profiles, the turbulence intensities are not self-similar as time proceeds. It is evident from figure 4($b$–$d$) that the present precomputation reproduced all these essential features. Figure 4($e$) presents profiles of the rate of turbulence kinetic energy dissipation. Spanwise energy spectra of the turbulence kinetic energy are given in figure 4($f$) for completeness. Note that the results in figure 4 are presented in the wake-coordinate system (see figure 2). The fluctuating wake velocities obtained from the precomputation are rescaled by the wake maximum deficit $u_{\text{wake, max}}$ and half-width $b$ before they are applied to (7). Using the experimental correlation of Schlichting (1979) for far wakes, at $x/L = 0.1$ $u_{\text{wake, max}} = 0.14U_{\text{ref}}$ and $b \approx 0.1L$ for the present flow conditions.

At the top surface of the computational domain the following boundary conditions were applied: $v = v_{\text{blasius}}$, $\partial u/\partial y = \partial v/\partial x$, and $\partial w/\partial y = \partial v/\partial z$. This is artificial, but given the substantial distance between the top surface and the wall, the effect of the

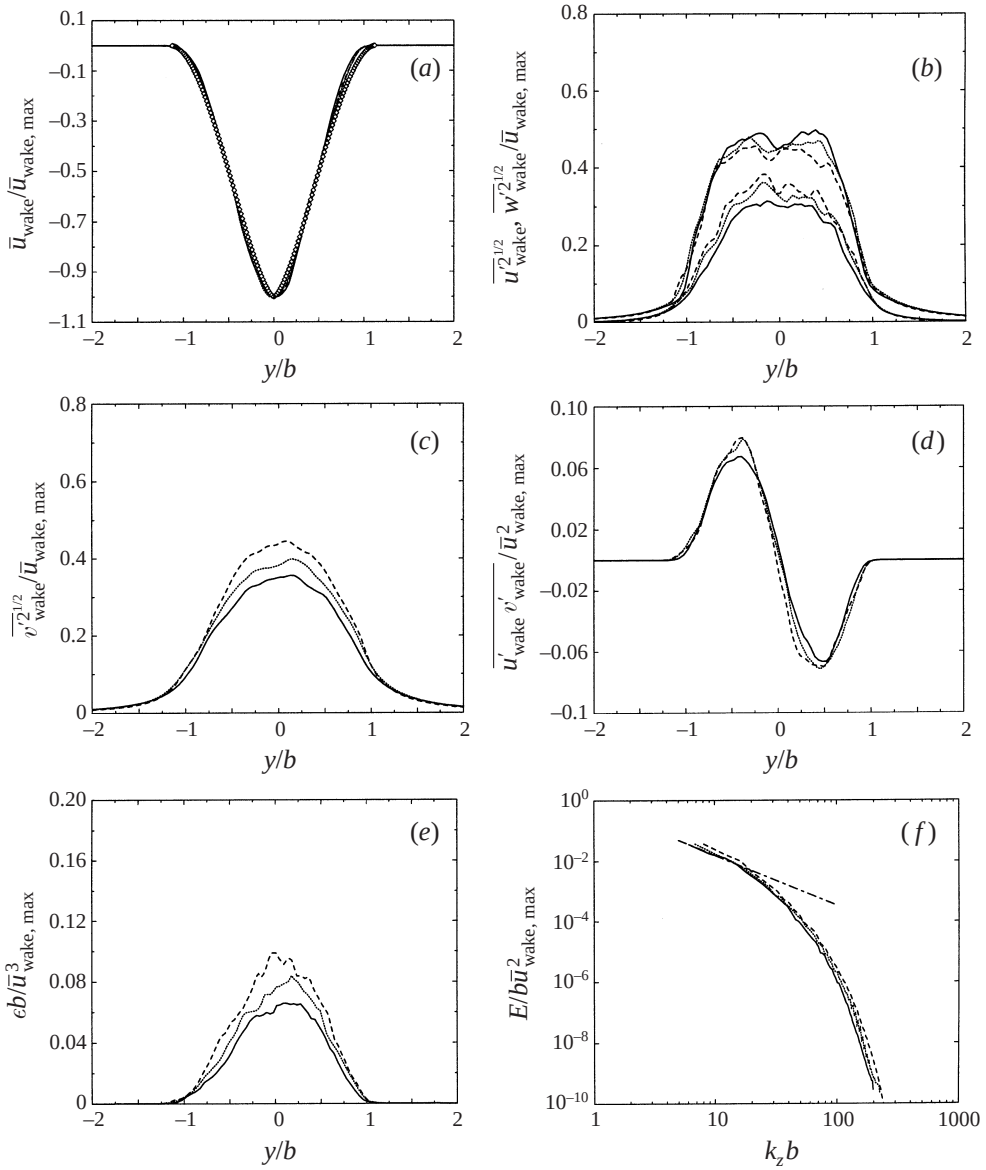


FIGURE 4. Characteristics of the simulated temporally decaying plane wake for the generation of inflow turbulence: ——, $\overline{u}_{\text{wake,max}} = 0.12$; ·····, $\overline{u}_{\text{wake,max}} = 0.10$; – – – –, $\overline{u}_{\text{wake,max}} = 0.08$; ◇, plane cylinder wake of Schlichting (1979); —·—, $E \propto k_z^{-5/3}$ law. (*a*) Mean velocity; (*b*) streamwise and spanwise fluctuations; (*c*) wall-normal fluctuations; (*d*) turbulent shear stress; (*e*) viscous dissipation rate of turbulence kinetic energy; (*f*) spanwise spectrum of turbulence kinetic energy.

top boundary condition on boundary layer development should be extremely small. At the exit of the computational domain, convective boundary conditions were used. Mass flux at the inflow plane was made constant in time by rescaling the velocities obtained from (7), and corrections to the velocities at the exit plane are also made to ensure global mass conservation. Periodic boundary conditions were applied in the homogeneous, spanwise $z$-direction; $\boldsymbol{u} = 0$ was applied on the wall.

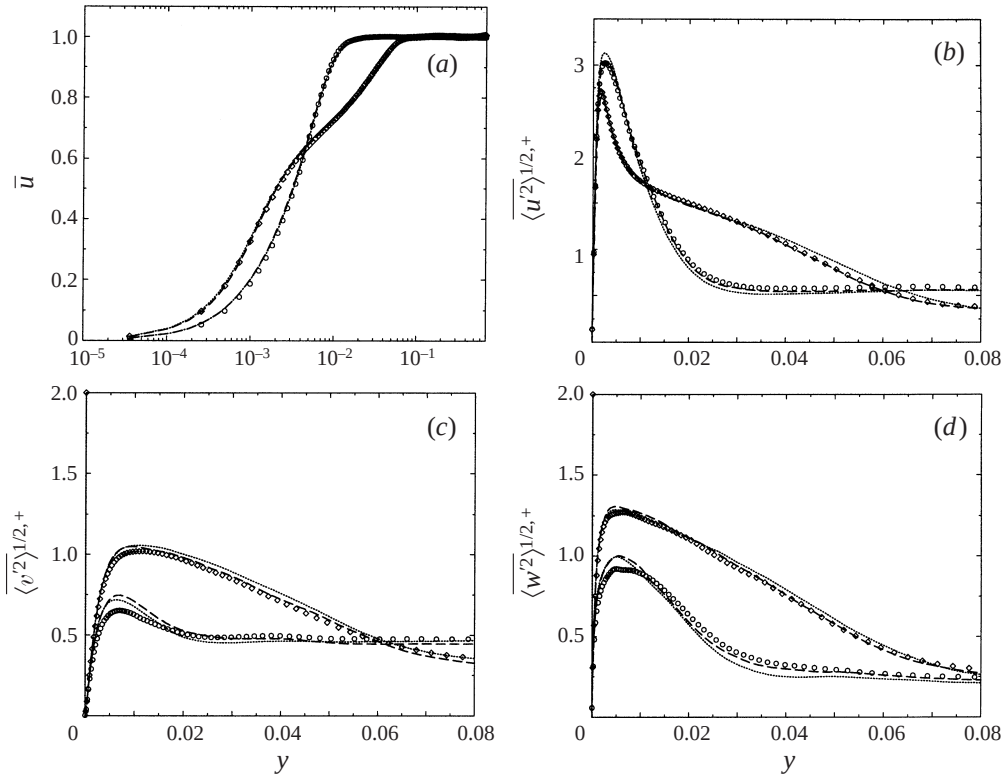


FIGURE 5. Resolution check: symbols, baseline case with $\Delta x^+_{x=3} = 24$ ($\Delta x^+_{x=1} = 18.3$) and $\Delta z^+_{x=3} = 11$ ($\Delta z^+_{x=1} = 8.4$): ○, during transition $x = 1.0$; ◇, after transition $x = 3.0$; ——, spanwise resolution refined by 50%; ·····, streamwise resolution coarsened by 50%.

### 2.4. *Numerical method*

The numerical scheme for the DNS is a parallelized version (by Charles D. Pierce at Stanford) of the method used by Akselvoll & Moin (1996) and Pierce & Moin (1998). Convection and diffusion terms that involve only derivatives in the wall-normal direction are treated implicitly, whereas all other terms are treated explicitly. All spatial derivatives are approximated with a second-order central difference scheme. A third-order Runge–Kutta scheme (Spalart, Moser & Rogers 1991) is used for terms treated explicitly and a second-order Crank–Nicolson scheme is used for terms treated implicitly. The fractional step method is used to remove the implicit pressure dependence in the momentum equations. Further details can be found in Akselvoll & Moin (1996). For parallel computation the computational domain is decomposed in two directions whereas a third direction is complete. When solving the Poisson equation using fast transforms, a transpose is necessary to switch the un-decomposed direction. Scalable parallelization is achieved using message passing interface (MPI) libraries.

### 2.5. *Computational details and resolution check*

The governing equations are solved on a rectangular staggered grid. The grid spacings are uniform in the streamwise and spanwise directions.

Simulation results to be presented in the following sections were obtained on a (1024, 400, 128) grid in the streamwise, wall-normal and spanwise directions, respec-

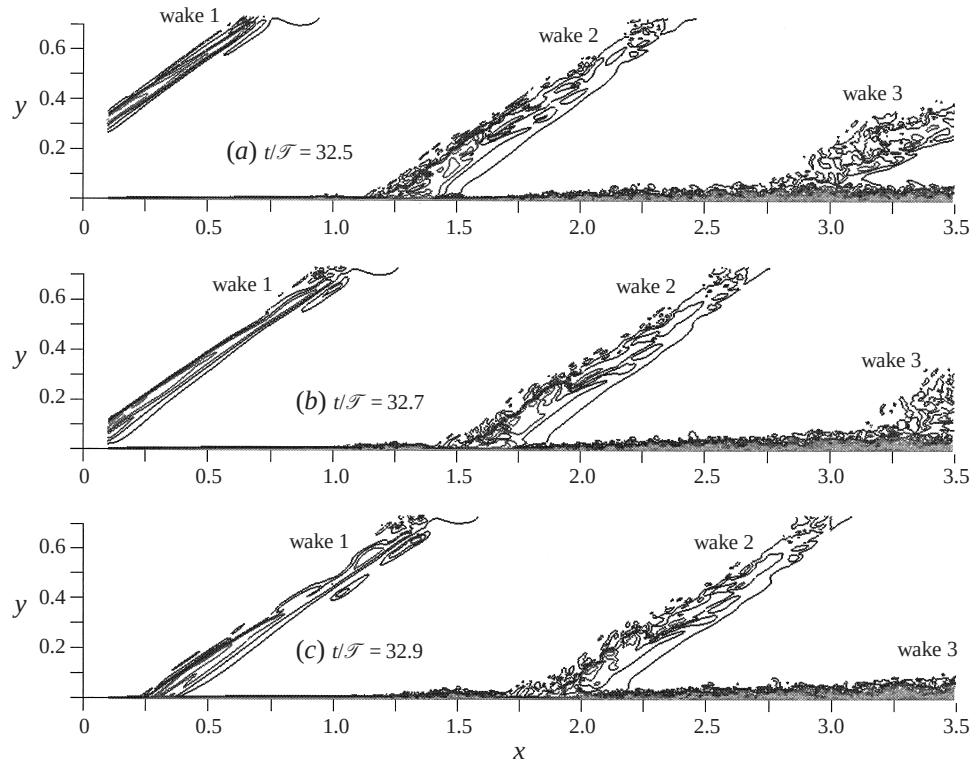


FIGURE 6. Contours of $u$ over one $(x, y)$-plane.

tively. The total of 52.4 million grid points is one of the largest that has ever been reported: compare to 11.0 million, 6.2 million and 17.3 million used by Spalart (1988), Yang, Spalart & Ferziger (1992) and Rai & Moin (1993), respectively.

In terms of viscous wall units based on the time-averaged local friction velocity after transition, $\Delta x^+_{x=3} = 24$ and $\Delta z^+_{x=3} = 11$. When measured using a friction velocity during transition, $\Delta x^+_{x=1} = 18.3$ and $\Delta z^+_{x=1} = 8.4$. At the exit, there are 16 points distributed along the wall-normal direction below $y^+ = 9$, and a total of 191 points below $y = \delta$. The resolution used in Spalart (1988) was $\Delta x^+ \approx 20 \pm 1$, $\Delta z^+ \approx 6.7 \pm 0.34$, with 10 points within 9 wall units.

In order to check the adequacy of the streamwise and spanwise grid resolution, two complete additional simulations were performed. It was difficult to use a grid size larger than (1024, 400, 128) due to memory constraints of the computer. Therefore, in the first additional simulation the spanwise dimension of the computational domain was reduced from $0.2L$ to $0.15L$, which is equivalent to $30\delta$ at the inlet, $3.94\delta$ in the middle of the plate and $2.18\delta$ at the exit. Even such a reduced spanwise dimension is still sufficiently wide and we therefore assume most of the differences, if any, between the two sets of results are due to the spanwise grid resolution change from $\Delta z^+_{x=1} = 8.4$ to $\Delta z^+_{x=1} = 6.3$. In the second additional simulation, the number of grid points in the streamwise direction was reduced by 50% from 1024 to 768. Except for these changes, all the other parameters were kept the same as the baseline simulation. Results from the resolution check are presented in figure 5. Figure 5($a$) compares the three sets of mean velocity profiles at two streamwise stations: the first, at $x = 1.0$, is in the transitional region; and the second, at $x = 3.0$, is in the turbulent region.

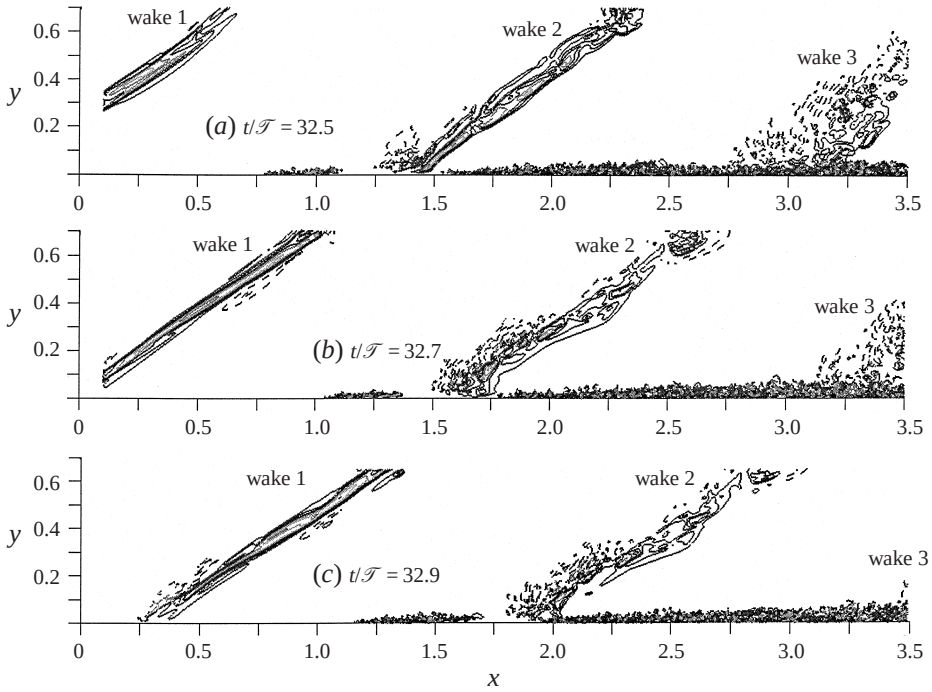


FIGURE 7. Contours of $v$ over one $(x, y)$-plane. In this and subsequent similar figures, negative values are contoured by solid lines; positive values are contoured by dashed lines.

The curves show good numerical resolution. Figures 5(*b*), 5(*c*) and 5(*d*) compare the streamwise, wall-normal and spanwise r.m.s. turbulent intensities, respectively. Differences among the three simulations are small. Additional resolution checks can be found in § 5. In addition to these resolution checks, we also build confidence on our simulation through extensive comparison, presented in § 5, with well-accepted DNS and experimental data. Comparison with the resolution used in previous channel flow turbulent spot simulations (e.g. Henningson & Kim 1991) gives further confidence that the present resolution is adequate. Years of turbulence simulation research at Stanford University has shown that, despite the slow convergence rate with grid refinement, second-order central differencing has several attractive features. It is energy conserving and does not carry inherent numerical diffusion, as do many high-order upwind biased schemes.

The time step was fixed to be $\mathrm{d}t = 10^{-3}\mathscr{T} = 0.00167L/U_{\mathrm{ref}}$, which is equivalent to $0.59\ \nu/\overline{u}^2_{\tau,x=3}$. Initial velocities were set to the laminar Blasius profile. The flow was then allowed to evolve for 20 wake passing periods (20 000 d$t$), and statistics were then collected for another 20 wake passing periods. Phase averaging was performed by dividing each pass period into 50 equal subdivisions. The computation was carried out on the scalable parallel Cray T3E at the Pittsburgh Supercomputing Center, using up to 512 processors.

## 3. Visualization of a matured turbulent spot

At the beginning of each period $t^m_{n\mathscr{T}} = 0$, the passing wake starts to enter the computational inflow plane at the top boundary $y = 0.8L$. Since the cylinder travels

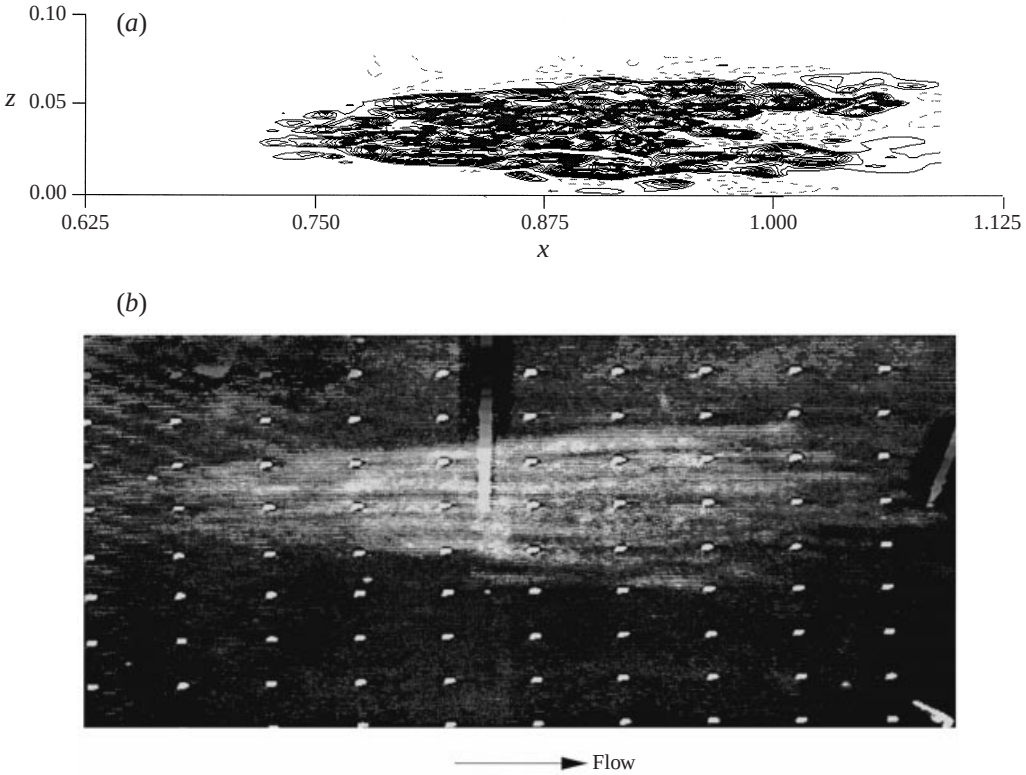


FIGURE 8. (*a*) Contours of $u'$ at $t/\mathscr{T} = 32.5$ over the $(x, z)$-plane $y = 7.38 \times 10^{-4}$ ($y^+ = 5.4$ at $x = 1.75$) – negative $u'$ represented by dashed lines; (*b*) visualization from the experiments of Zhong *et al.* (1998).

at $-0.7U_{\text{ref}}$, it takes $1.143L/U_{\text{ref}}$ or $0.684\mathscr{T}$ before the wake reaches the flat plate. After entering the computational domain, the wake is advected at the reference velocity $U_{\text{ref}}$ in the free stream and interacts with the boundary layer in the near-wall region. An important grid resolution requirement is that it be adequate to ensure that no vorticity is spuriously left in the free stream after the wake has passed.

An overall view of the wake evolution as it is advected along the plate and the laminar to turbulent transition can be seen in figures 6 and 7. Figure 6 presents contours of instantaneous streamwise velocity over one random $(x, y)$-plane at three consecutive instants: $t = 32.5\mathscr{T}$, $32.7\mathscr{T}$ and $32.9\mathscr{T}$. It is seen from the figure that in the free stream the wake angle remains the same at all the three instants, and that there is no residual velocity gradient left by the passing wake. The small effects of the upper boundary show that the computational domain is sufficiently high compared to the boundary layer thickness. Between the wakes the near-wall velocity contours from the inlet to $x \approx 1.0$ are straight, indicating that the flows in these moving regions are predominantly laminar. Beyond $x = 1.75$ the contours are chaotic in the near-wall region at all the instants, and there is also apparent thickening in the boundary layer. This indicates that laminar-to-turbulent transition has been nearly completed.

Figure 7 presents contours of instantaneous wall-normal velocity $v$ at the same locations and instants as in figure 6. The wall-normal velocity inside the wake is significantly larger than that in the free stream of a normal laminar or turbulent boundary layer because of the wake angle $\alpha$. The figure shows that downstream

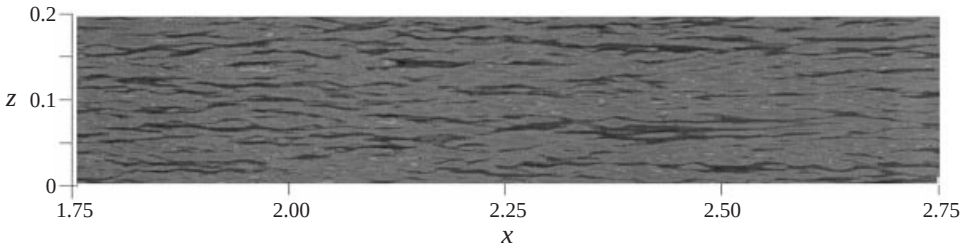


FIGURE 9. Contours of $u'$ at $t/\mathscr{T} = 32.5$ over the $(x, z)$-plane of $y = 7.38 \times 10^{-4}$ ($y^+ = 5.4$ at $x = 1.75$) showing turbulent streaks in the turbulent region – negative $u'$ represented by darker contours.

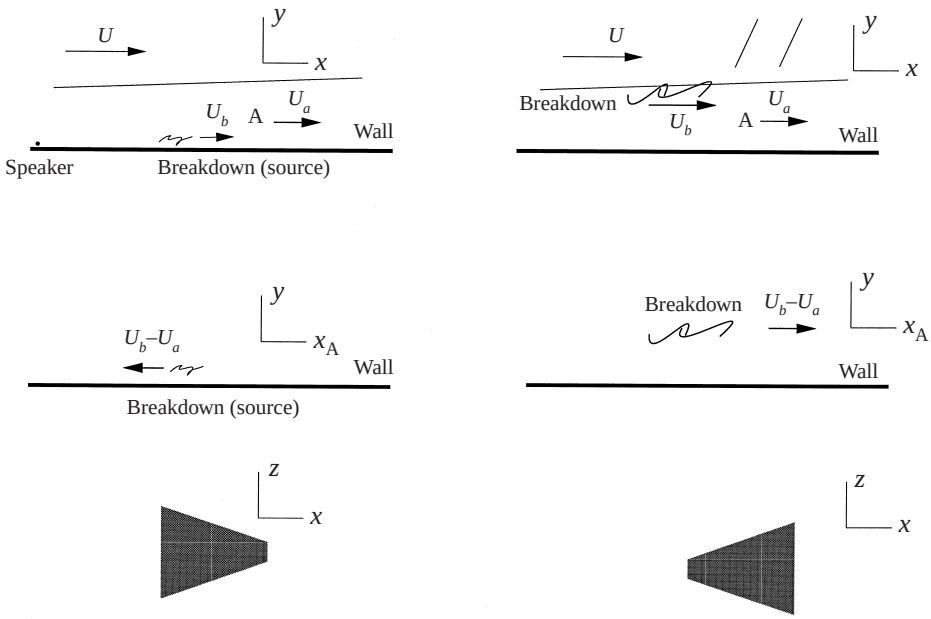


FIGURE 10. One possible reconciliation of the spot arrowhead direction found in the present study with that in previous boundary layer studies.

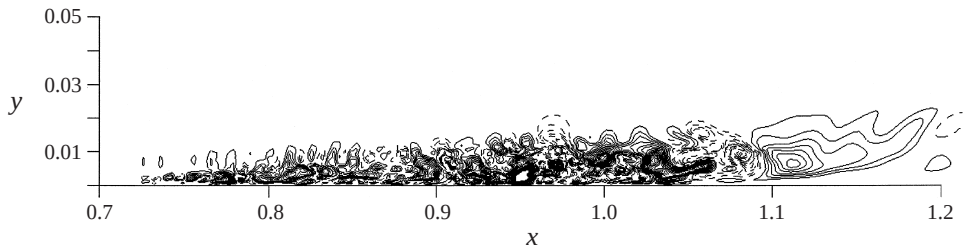


FIGURE 11. Side-view of the turbulent spot at $t/\mathscr{T} = 32.5$ over the $(x, y)$-plane of $z = 0.03$: ——, $-0.20U_{\text{ref}} < v' < -0.01U_{\text{ref}}$; - - - -, $0.01U_{\text{ref}} < v' < 0.20U_{\text{ref}}$; increment $0.005U_{\text{ref}}$.

of $x \approx 2.0$ the instantaneous wall-normal velocity is chaotic near the wall, with substantial magnitude all the time, as would be found inside a turbulent boundary layer. It is interesting to note that, upstream of $x \approx 1.75L$, an isolated spot near the wall containing large-amplitude and chaotic vertical velocities is developing on

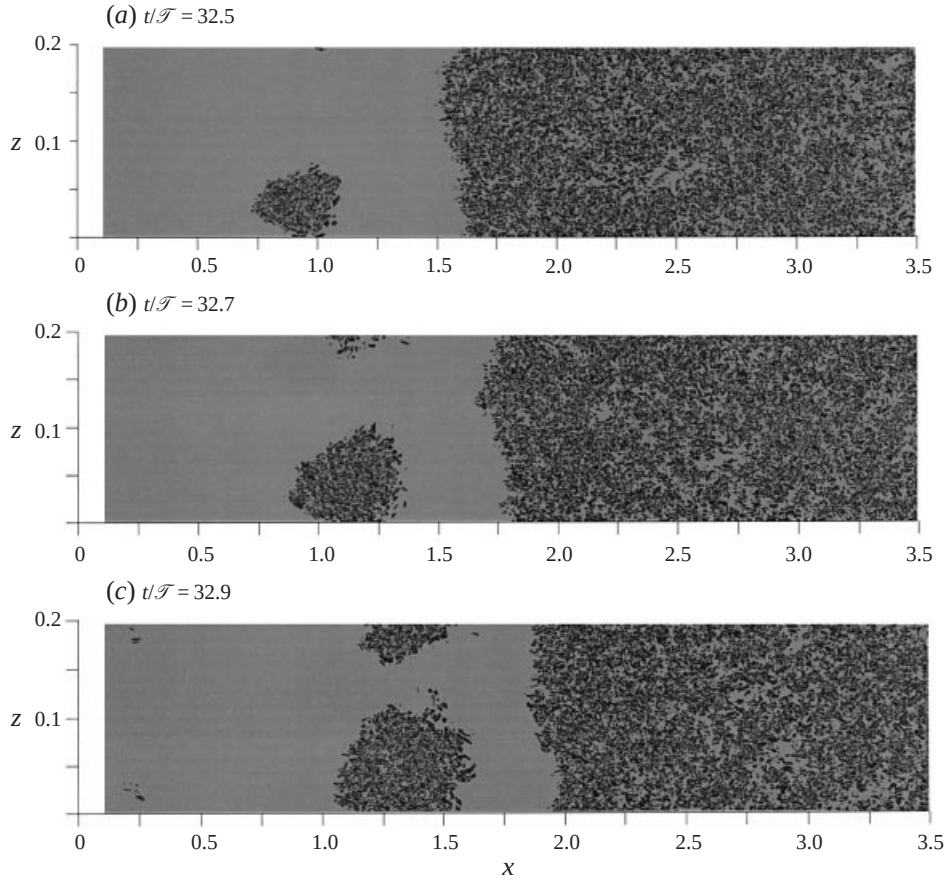


FIGURE 12 (*a–c*). For caption see facing page.

the upstream side of the free-stream wake. It can be seen from the contours that as the spot propagates downstream, its streamwise dimension lengthens. The evolution of this particular turbulent spot, as well as its connection to the overall unsteady boundary layer transition, will be examined in the remainder of this subsection.

Figure 8(*a*) provides a close-up plan view of the turbulent spot indicated by figure 7(*a*). Shown in the figure are contours of $u'$ at $t = 32.5\mathscr{T}$ over the $(x, z)$-plane of $y = 7.38 \times 10^{-4}$. The spot has an arrowhead shape pointing upstream, with streamwise elongation. Because $u'$ represents turbulence fluctuations with respect to the phase-averaged mean, the contours are predominantly positive inside the spot. If $u'$ is computed with respect to a conditional mean, averaged only inside the spot, there will be both positive and negative fluctuations. This can also be inferred from the high-speed and low-speed streaks inside the spot in figure 8(*a*). Figure 8(*b*) presents a flow visualization picture obtained by Zhong *et al.* (1998) in an experimental configuration similar to ours (figure 2*b*). Good agreement between the DNS spot and the experimental visualization is evident. Figure 9 shows contours of $u'$ at the same time and $(x, z)$-plane as in figure 8(*a*), but within a further downstream, fully turbulent region. The most distinctive feature found in the figure is the existence of low- and high-speed streaks. These streaks and their associated streamwise vortices have been recognized as a signature of fully developed near-wall turbulence (Hamilton, Kim &

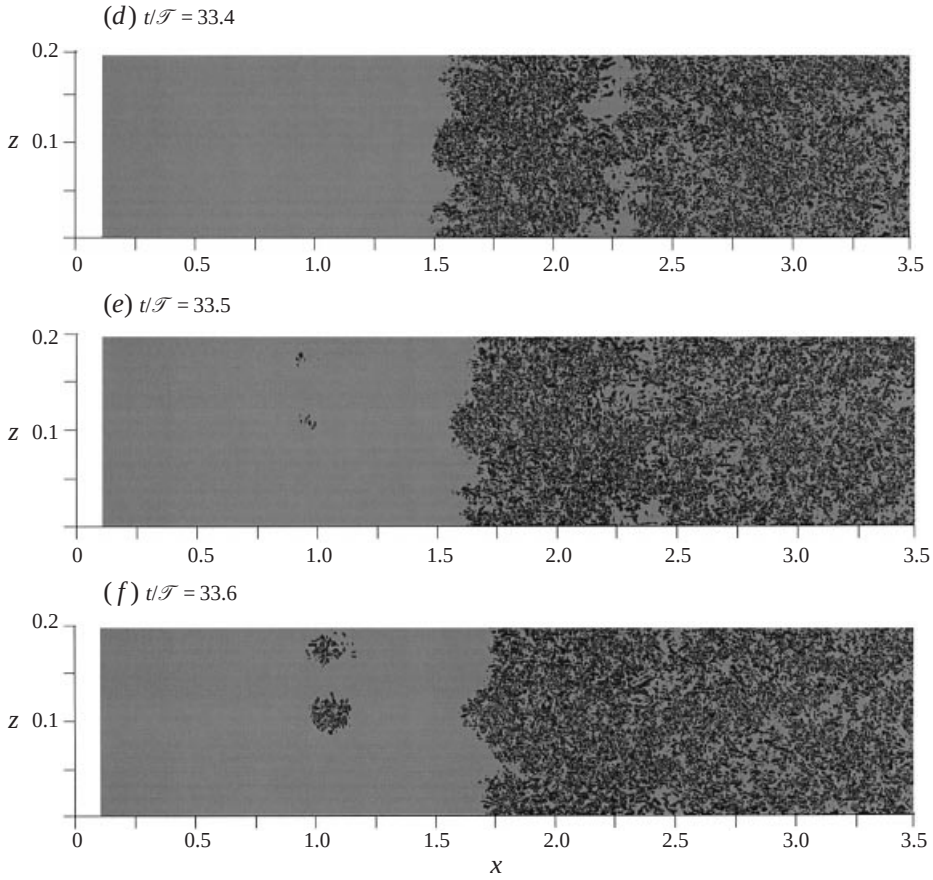


FIGURE 12. Visualization of spot growth and transition to turbulence using $v'$ over the $(x, z)$-plane of $y = 7.38 \times 10^{-4}$ ($y^+ = 5.4$ at $x = 1.75$); contours represent $0.005U_{\text{ref}} \leqslant |v'| \leqslant 0.2U_{\text{ref}}$ with increment $0.005U_{\text{ref}}$.

Waleffe 1995). The commonly accepted characteristic wavelength of such streaks is about 100 wall units. The entire spanwise dimension in figure 9 is about 1400 wall units. Such turbulent streaks should not to be confused with the puffs existing in the laminar region prior to the occurrence of turbulent spots, as drawn in figure 3.

Our turbulent spot and that of Zhong *et al.* (1998) have an arrowhead pointing upstream, in the reverse direction to that reported in many previous boundary layer studies (Henningson, Spalart & Kim 1987; Jahanmiri, Prabhu & Narasimha 1996). This discrepancy is too glaring to be left uncommented on.

Figure 10 depicts a simple rationale for the difference. The breakdown fluid parcels contain the 'source' of turbulence, which is spread to form a spot as the parcels themselves are convected downstream. In many previous boundary layer turbulent spot studies breakdown takes place near the wall, where the local convection velocity is small. At the position, A, located higher above the wall than the source, the turbulent fluid parcels travel downstream relative to the source. At any given instant fluid parcels at smaller $x_A$ have a longer time to spread laterally, thus forming an arrowhead pointing downstream.

Breakdown provoked by free-stream turbulence occurs in the outer part of the layer where the local convection velocity is large (see § 4 for further discussion). In the reference frame of observer A, nearer to the wall than the breakdown location, the highly turbulent breakdown fluid parcels are convected downstream. At any given instant, fluid parcels at larger $x_A$ have had longer to spread laterally, thus forming an arrowhead pointing upstream. Alternatively, in the frame of reference of the source, the boundary layer flow is increasingly in the $-x$-direction as the wall is approached. Thus the spot is sheared towards the upstream direction near the wall: the vertical section in figure 11 illustrates this structure.

Evolution of a turbulent spot and the process of unsteady periodic transition is portrayed in figure 12. Presented in this figure are visualizations of the instantaneous wall-normal fluctuation $v'$ over the $(x, z)$-plane, $y = 7.38 \times 10^{-4}$, which is equivalent to $y^+_{x=1.75} = 5.4$. A total of six consecutive realizations are given from $t = 32.5\mathscr{T}$ to $t = 33.6\mathscr{T}$, covering more than a full wake passing period. In the figure, the background is used to represent negligible fluctuations with $-0.005 \leqslant v' \leqslant 0.005$. Other contours represent stronger fluctuations $0.005 < |v'| < 0.2$ with an increment of 0.005. Note that the spanwise dimension in figure 12 has been magnified by a factor of four in order to show the full streamwise dimension. The spot appearing in figure 12(*a*) is the same as that presented in figure 8(*a*), except that the contours are now drawn using $v'$. Because of the enlarged $z$-dimension, the spot dimensions are distorted. Their real physical shape is as in figure 8(*a*).

In figure 12(*b*) a small patch of large turbulent fluctuations exists near the upper boundary ($z \approx 0.2$, $x \approx 1.0$). This is part of the wing tip of the turbulent spot near the lower boundary, extended via the periodic boundary condition in the spanwise direction. From $t = 32.5\mathscr{T}$ to $32.7\mathscr{T}$ the arrowhead of the turbulent spot broadens, but is still pointing upstream. In the meantime the flank of the spot becomes sharper, making a well-defined angle with respect to the flow direction. As the wing tip expands, more fluctuations stronger than the background level are seen to appear near $z = 0.2$ as well. Along the $z = 0$ boundary, the downstream turbulent region retreats from $x \approx 1.65$ at $32.5\mathscr{T}$ to $x \approx 1.75$ at $32.7\mathscr{T}$.

At $t = 32.7\mathscr{T}$ the next wake starts to touch the flat plate. Large turbulence fluctuations advected into the near-wall region of the computational domain by the wake can be seen in figure 12(*c*) near $x = 0.25$. These fluctuations decay rapidly so that in figure 12(*d*) they have entirely disappeared. This provides evidence that turbulent spots are not produced immediately where impact occurs.

From $t = 32.7\mathscr{T}$ to $32.9\mathscr{T}$, the shape of the turbulent spot transforms from a well-defined wedge to a two-dimensional strip. This process occurs through a rapid increase in the angle which the flank makes with the streamwise direction. Eventually the arrowhead shape disappears, resulting from a tendency towards equalization of the dimensions of the leading and trailing edges of the spot.

Formation of a full two-dimensional strip, and catching up the downstream turbulent region by the strip, are shown in figure 12(*d*). The two-dimensional strip does not extend over the whole spanwise dimension until $t = 33.4\mathscr{T}$, nearly 0.9 passing period after the appearance of the spot in figure 12(*a*). Relative to the given passing frequency, the evolution from isolated turbulent spots to a full two-dimensional strip is rather gradual. Prior to being caught by the turbulent strip, the continuously turbulent region had moved to $x \approx 2.4L$; through the act of being caught, the continuously turbulent region jumps back to $1.6L$, restoring its position of figure 12(*a*). The transition cycle is begun anew by the emergence of two small turbulent spots near $x \approx 0.9L$ in figure 12(*e*). Figure 12(*f*) shows the state of these two young turbulent spots after another 0.1 passing period.

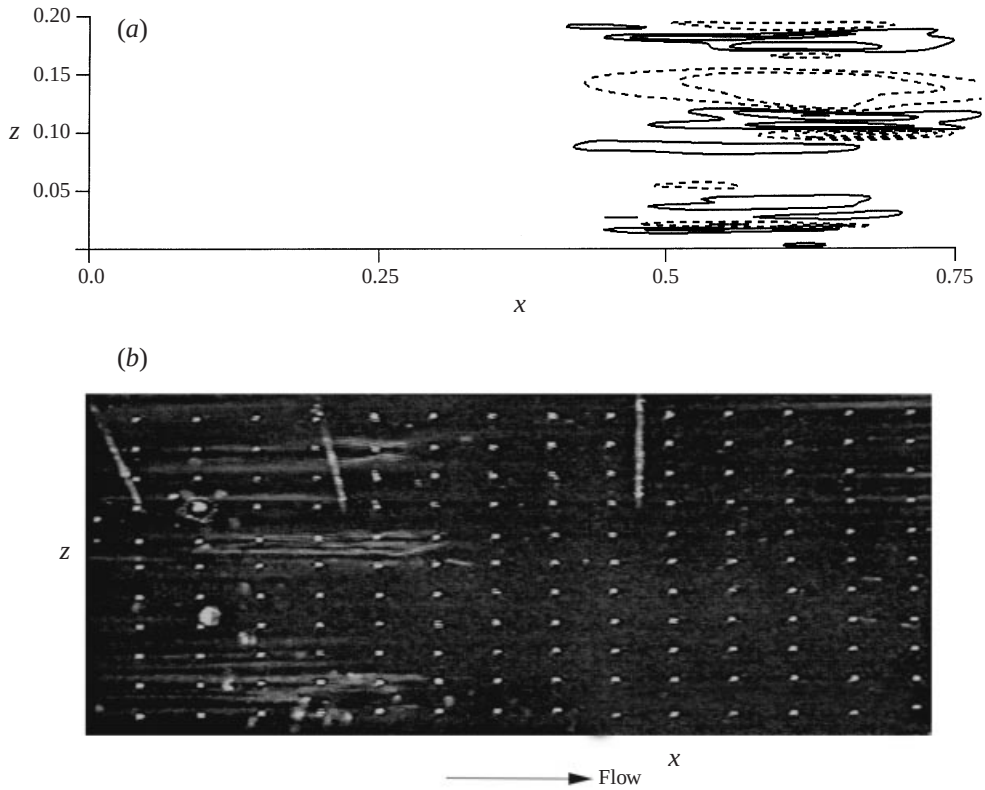


FIGURE 13. 'Puff' prior to the emergence of turbulent spot: (*a*) $u'$ at $t/\mathscr{T} = 33.2$ over the $(x, z)$-plane of $y = 7.38 \times 10^{-4}$ ($y^+ = 5.4$ at $x = 1.75$). (*b*) Visualization from the experiments of Kittichaikarn *et al.* (1999).

## 4. The search for the origin of a young turbulent spot

We have argued in § 1 and § 3 that inlet disturbances develop into streaky structures (puffs) inside the boundary layer. Selective amplification of the puffs in the transitional region occurs when certain types of free-stream wake eddies interact with boundary layer flow. Breakdown starts near the boundary layer edge. We are now ready to provide supportive evidence for this argument.

Figure 13(*a*) demonstrates the existence of streaky structures in the transitional region. Shown in the figure are $u'$ contours at $t = 33.2\mathscr{T}$ over the same $(x, z)$-plane as in figure 12. This particular instant is $0.3\mathscr{T}$ prior to the emergence of young spots in figure 12(*e*). The elongated positive and negative $u'$ contours resemble the puff sketched in figure 3, and are essentially the same as those observed by Alfredsson & Matsubara (1996) in a boundary layer under continuous free-stream turbulence. Figure 13(*b*) presents one interesting flow visualization picture obtained by Kittichaikarn *et al.* (1999) that compares favourably with our simulation. The three streaky structures are precursors of turbulent spots. Additional visualizations show the occurrence of three well-defined turbulent spots some time following figure 13(*b*).

Figure 14 follows the three puffs of figure 13(*a*) through their earlier history. It starts with their inception, near the inlet, and follows them to their ultimate breakdown

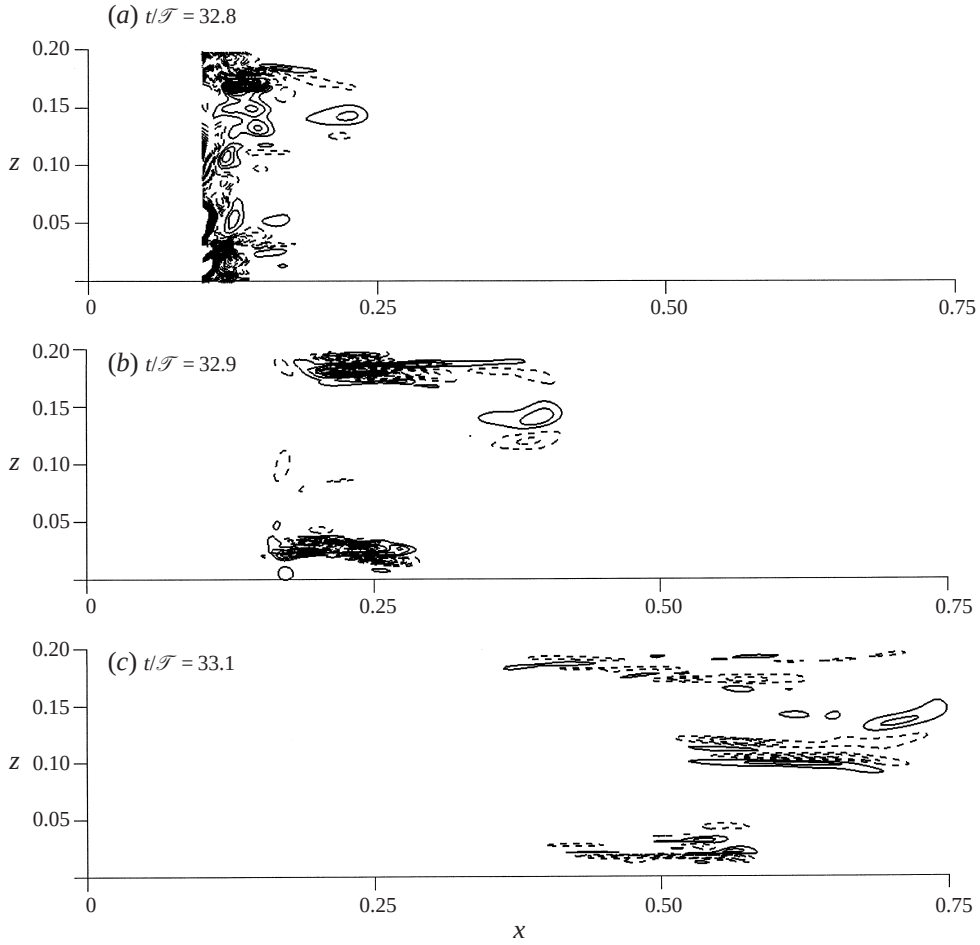


FIGURE 14 (*a–c*). For caption see facing page.

near $x = 1.0$. That is the point of the emergence of young spots in figure 12(*e*). In this figure the contour plots of $v'$ have the threshold level reduced by a factor of ten compared to figure 12 (from 0.005 to 0.0005). Near-wall inlet wake disturbances shown in figure 14(*a*) rapidly evolve into three patches in figure 14(*b*). Each of these three patches is made of elongated structures with upward and downward motions, suggesting an association with streamwise vortices. Figure 14(*c*) shows that the top puff (near $z = 0.175$) and lower puff (near $z = 0.025$) decay from $32.9\mathscr{T}$ to $33.1\mathscr{T}$, whereas the middle puff (near $z = 0.1$) intensifies. Attenuation or amplification of the near-wall puff is dependent upon the type of forcing from free-stream eddies. Figure 15 illustrates such forcing. Figure 15(*a*) shows $u'$ in an $(x, y)$-plane cut through the centre of the top puff, at an instant midway between figure 14(*b*) and figure 14(*c*). The time-averaged boundary layer thickness in this region is about 0.006. Positive $u'$ are found behind the wake inside the boundary layer ($0.25 < x < 0.4$), implying the absence of inflectional instability. Figure 15(*c*) shows $u'$ in an $(x, y)$-plane cut through the centre of the lower puff. Again, positive $u'$ is evident. The lack of forcing through inflectional instability in figures 15(*a, c*) corresponds to the decay of the top

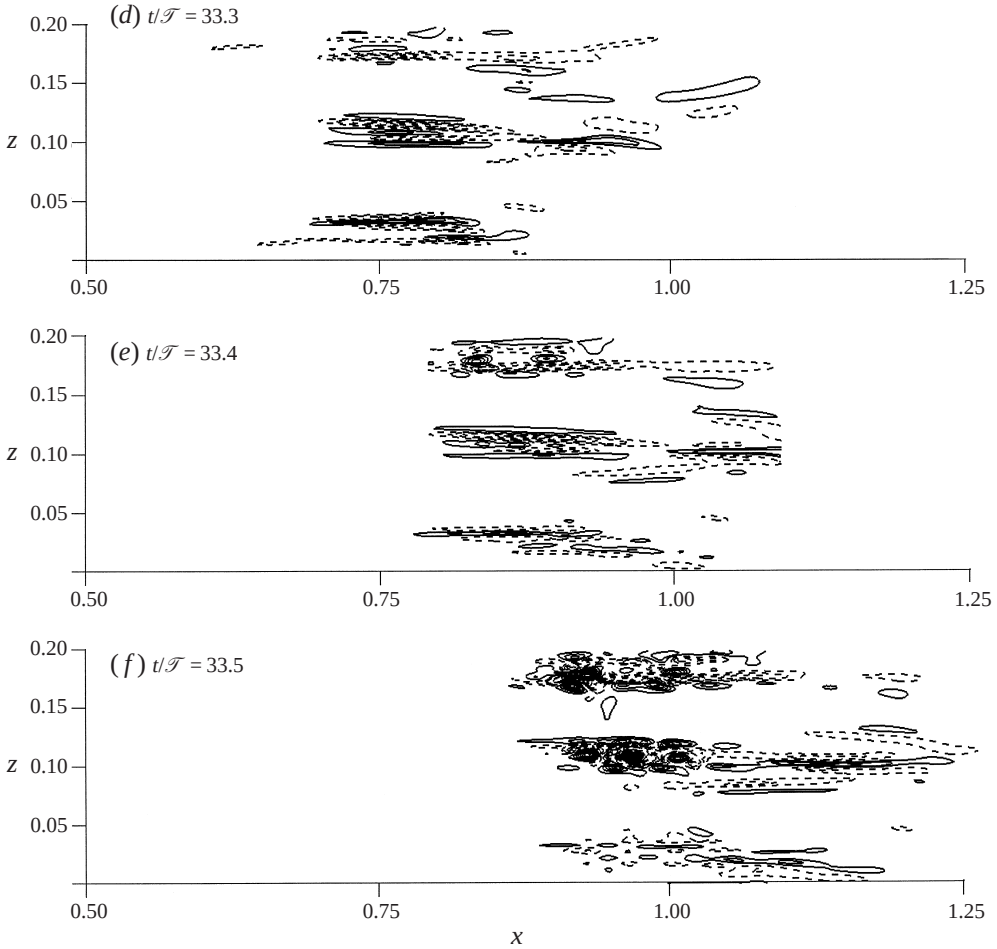


FIGURE 14. Visualization of the evolution of puffs and breakdown to young turbulent spots using $v'$ over the $(x, z)$-plane of $y = 7.38 \times 10^{-4}$ ($y^+ = 5.4$ at $x = 1.75$); $0.0005U_{\text{ref}} \leqslant |v'| \leqslant 0.008U_{\text{ref}}$ with increment 0.0005.

and lower puff shown in figure 14($c$). Figure 15($b$) presents contours of $u'$ in an $(x, y)$-plane cut through the centre of the middle puff. Evident from the figure are the negative $u'$ contours in the region where free-stream wake eddies interact with boundary layer flow. This corresponds to the amplification of the middle puff seen in figure 14($c$).

Figure 14($d$–$f$) shows variations of the three puffs before breakdown. The trend toward attenuation of the top puff is reversed. This is because the free-stream forcing shown in figure 16($a$) is of the opposite sign to that in figure 15($a$). $u'$ is strongly negative. Strong negative $u'$ is also seen in figure 16($b$). Under such forcing, the top and middle puff break up at $t = 33.5\mathscr{T}$. In contrast, figure 16($c$) shows there is very weak forcing in the lower puff. This corresponds to its monotonic decay as seen in figure 14($b$–$f$). Figure 17 visualizes the evolution of the three puffs by way of contours of streamwise fluctuations.

Figure 18 shows the breakdown using contours of $u'$. Again, the three $(x, y)$-planes $z = 0.175$, 0.11 and 0.025 cut through the centres of the three puffs. Due to the negative $u'$, the boundary layers in figure 18($a$) and figure 18($b$) have inflectional

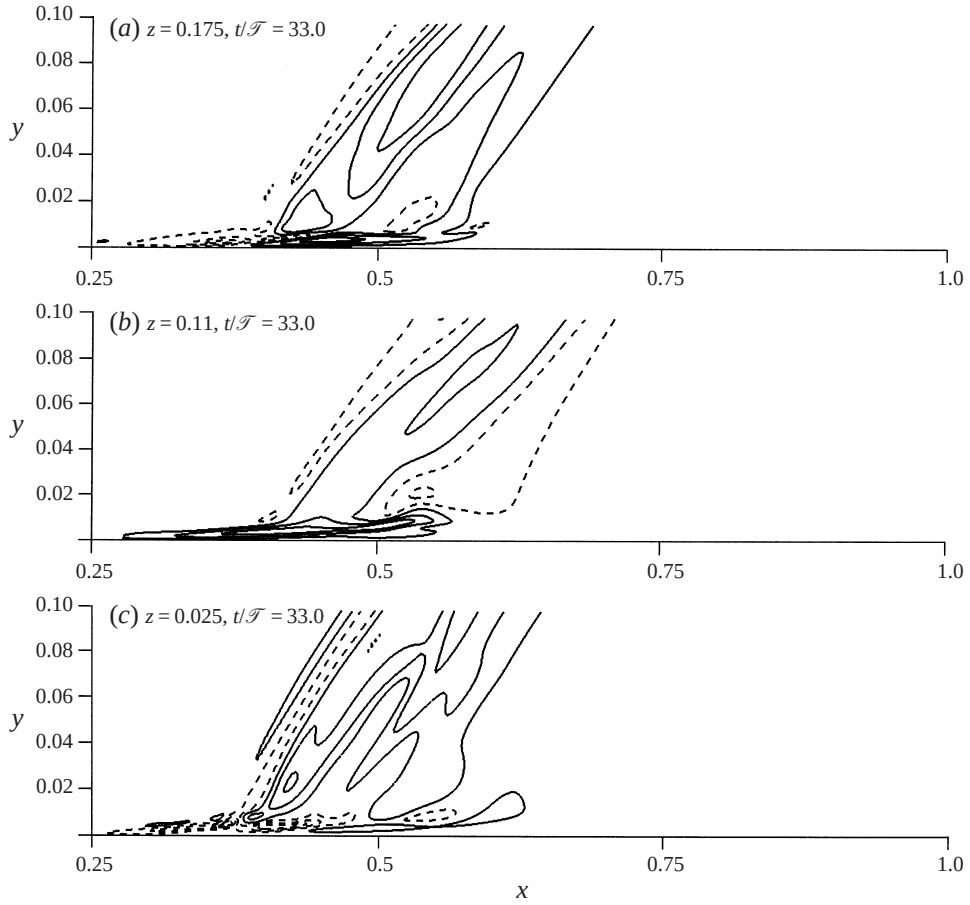


FIGURE 15. Visualization of the forcing by free-stream eddies through localized instability using $u'$ over three $(x, y)$-planes at $t/\mathscr{T}=33.0$; $0.02U_{\text{ref}} \leqslant |u'| \leqslant 0.34U_{\text{ref}}$ with increment 0.04.

profiles. The wavy structures in the velocity field are the signature of their instability. Figure 18(*b*) suggests that breakdown occurs first in the outer part of the layer. When breakdown takes place, the negative streamwise fluctuations are replaced by positive fluctuations (compare figure 18(*b*) and figure 19(*b*) at $x = 1.0$). A turbulent spot is made of predominantly positive $u'$ (see figure 8*a*), thus high local skin friction. Near the downstream end of the turbulent spot, positive $u'$ of the spot collides with negative $u'$ associated with the forcing (see figure 19*b* at $x = 1.05$). Continuity thus results in a high positive wall-normal fluctuation $v'$ in this region. The strong upward motion near the downstream end of the spot results in an overhang, which is clearly visible in figure 7(*c*).

One final observation to be made is that figure 18(*b*) shows more conclusively that breakdown starts from the outer layer than figure 18(*a*). Our reasoning in § 3 concerning the arrowhead direction of the spot associated with the middle puff is that it should have a more well-defined arrowhead pointing upstream than the top one. This is indeed the case. See the two young spots in figure 12(*f*) and note again that the spanwise dimension has been enlarged by a factor of four.

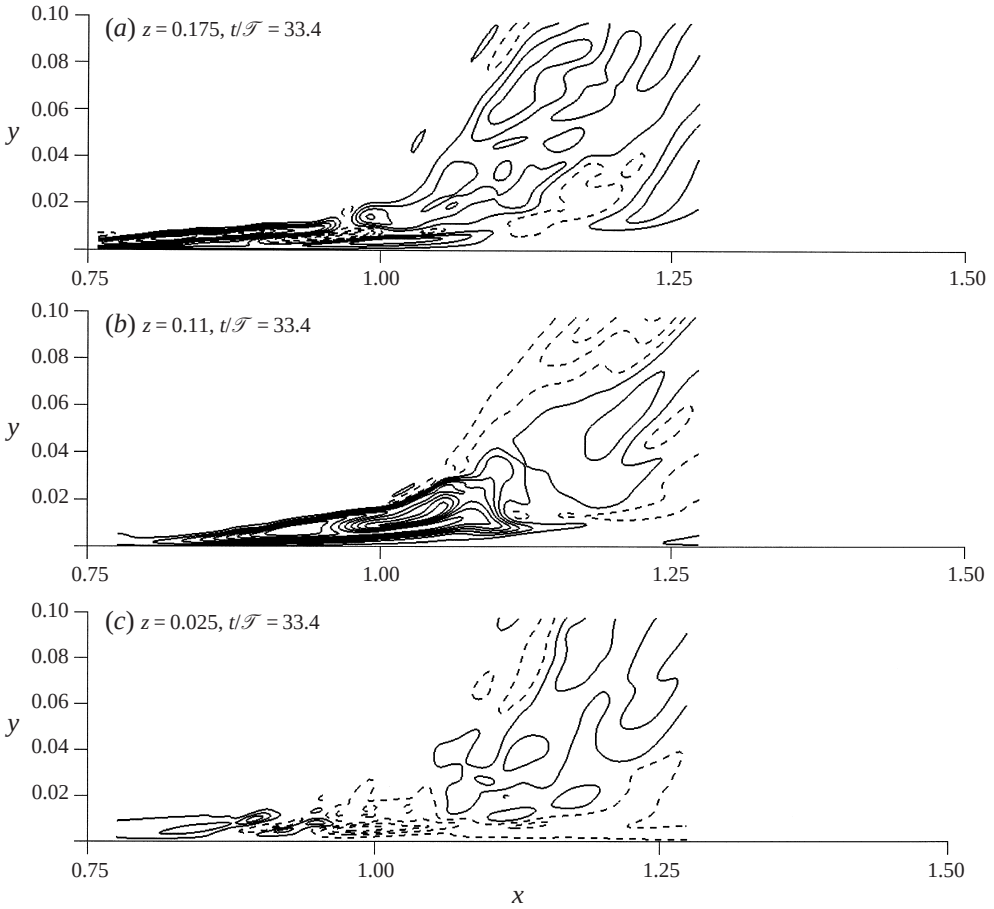


FIGURE 16. Visualization of the forcing by free-stream eddies through localized instability using $u'$ over three $(x, y)$-planes at $t/\mathscr{T}$=33.4; $0.02U_{\text{ref}} \leqslant |u'| \leqslant 0.34U_{\text{ref}}$ with increment 0.04.

## 5. Time-averaged boundary layer properties

Time-averaged boundary layer integral parameters are presented in figure 20. In addition to the laminar Blasius solution, two sets of DNS results are shown: the simulation with $\Delta z^+_{x=3} = 11$ and an additional simulation with $\Delta z^+_{x=3} = 8.25$. The laminar-flow momentum thickness Reynolds number $Re_\theta$ is 80 at the inflow station ($x = 0.1$). This is dictated by the assumption that the Blasius boundary layer is initiated from the leading edge with the prescribed length Reynolds number. At the exit of the computational domain ($x = 3.5$) the turbulent boundary layer has $Re_\theta = 1120$. It is seen from the figure that upstream of $x \approx 0.75$ the simulations follow the Blasius solution quite nicely with only very small deviations. The minor differences are due to the impact of the wake on the flat plate. Onset of transition starts at about $x \approx 0.7$ and by $x \approx 2.0$ the shape factor has dropped from 2.59 to 1.45. Further downstream the shape factor remains nearly the same, decreasing only slightly from 1.45 to 1.42 at the exit. Coles' (1956) correlation shows that in a turbulent boundary layer the shape factor drops from 1.48 at $Re_\theta = 600$ to 1.44 at $Re_\theta = 1100$.

Quantitative time-averaged skin-friction data are not available in most experiments

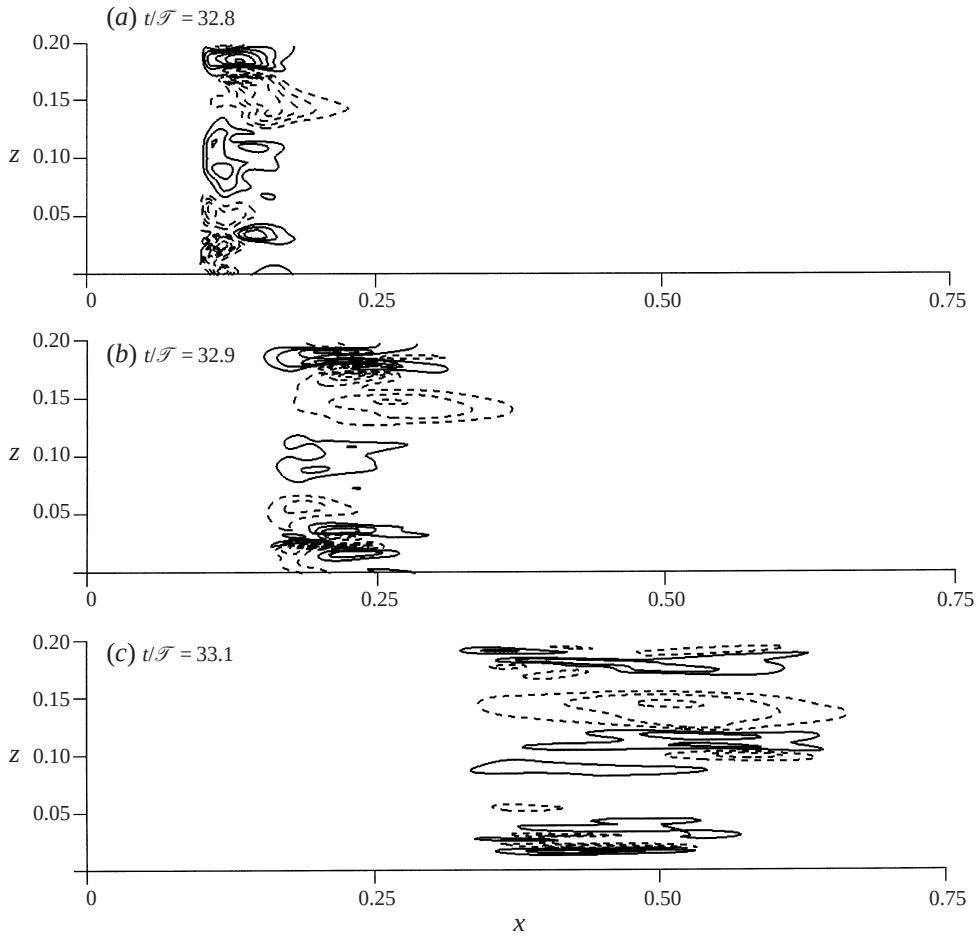


FIGURE 17 (*a–c*). For caption see facing page.

on wake-induced transition. Nevertheless, wall shear stress information is crucial since it provides an important velocity scale for boundary layer theory as well as a necessary quantity for engineering drag estimation. Figure 21 shows $C_f$. Similar to the previous figure, the Blasius solution and the results from the two simulations are presented. Within $0.1 \leqslant x \leqslant 0.5$, profiles of the computed skin-friction coefficient follow the Blasius solution with only a minor over-shoot near the inlet because of the impact of the wake on the flat-plate. $C_f$ starts to rise beyond $x \approx 0.7$ and attains a maximum at approximately 2.15. The streamwise location of the maximum skin friction may be used as a convenient, well-defined, indicator for the completion of the transition process. As will be shown next, time-averaged mean streamwise velocity and Reynolds shear stresses attain their corresponding fully turbulent profiles at approximately the same streamwise station. At the exit, $x = 3.5$, the computed skin-friction coefficient $C_f$ is 0.00479, 10% higher than that given by Coles' correlation. Free-stream turbulence fluctuations, such as those carried by the passing wake in the present case, tend to increase skin-friction (Hancock & Bradshaw 1989).

Time-averaged streamwise velocities at seven streamwise stations are shown in figure 22. Figure 22(*a*) plots $\overline{u}^+$ in inner coordinates. The three profiles upstream of $x =$

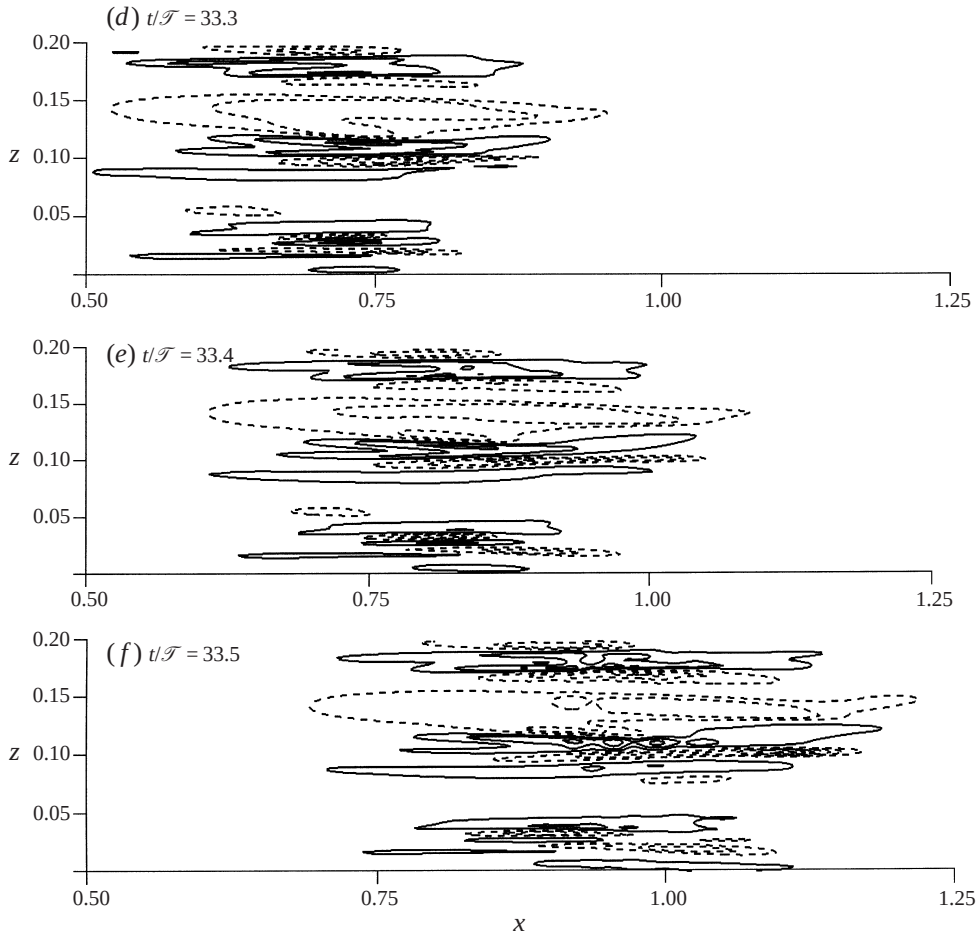


FIGURE 17. Visualization of the evolution of puffs using $u'$ over the $(x, z)$-plane of $y = 7.38 \times 10^{-4}$ ($y^+ = 5.4$ at $x = 1.75$); $0.02U_{\text{ref}} \leqslant |u'| \leqslant 0.14U_{\text{ref}}$ with increment 0.02.

1.5 display large deviations from the standard logarithmic profile $u^+ = 2.44 \ln y^+ + 5.0$, though the degree of deviation decreases along the streamwise direction. At $x = 2.0$ the profile of $\overline{u}^+$ still does not possess a well-defined logarithmic slope, indicating that on average transition is not complete at this station. Further downstream, the three profiles at $x = 2.5$, 3.0 and the exit (3.5) nearly collapse within $0 \leqslant y^+ \leqslant 300$. In the viscous region they follow the law of the wall $u^+ = y^+$. In the logarithmic region the slopes of these profiles are in excellent agreement with that of the log law, i.e. $1/\kappa$ with $\kappa = 0.41$. The intercept of the profiles is lower than the standard value 5.0 by approximately 0.8. This might be attributed to the higher time-averaged skin-friction value discussed in figure 21. The logarithmic velocity profiles produced by the present simulation are clearly defined. Interestingly, the 'wake' component (Coles 1956) in the outer part of the boundary layer is also well-defined even though Hancock & Bradshaw (1989) showed this tends to be suppressed when the intensity of free-stream turbulence exceeds the friction velocity $u_\tau$. Our numerical experiments show that the absence or existence of Coles 'wake' component depends upon wake orientation and passing frequency (see Wu & Durbin 1999*b* for further discussion).

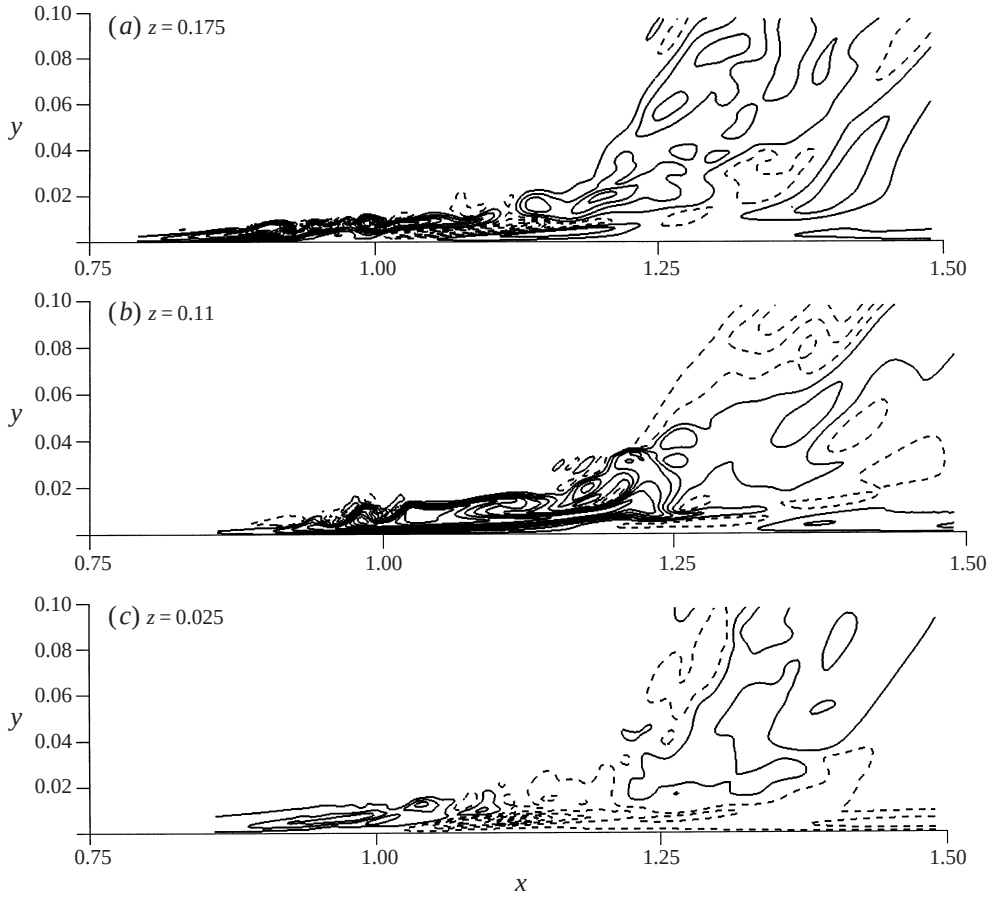


FIGURE 18. Visualization of the forcing by free-stream eddies through localized instability using $u'$ over three $(x, y)$-planes at $t/\mathscr{T}=33.5$; $0.02U_{\text{ref}} \leqslant |u'| \leqslant 0.34U_{\text{ref}}$ with increment 0.04.

Figure 22($b$) plots $\overline{u}/U_{\text{ref}}$ in outer coordinates. Also shown in the figure are the experimental measurements of Webster, DeGraff & Eaton (1996) on a flat plate at $Re_\theta = 1500$. In the transitional region, the profiles of $\overline{u}/U_{\text{ref}}$ become fuller with the increase of streamwise coordinate. A noticeable characteristic of these profiles is that velocities in the inner and outer regions of the boundary layer approach the fully turbulent experimental data differently. Close to the wall $\overline{u}$ increases monotonically with $x$. However, there is an over-shoot of $\overline{u}$ in the outer region of the boundary layer. The degree of over-shoot is the largest at $x = 1.5$, where the boundary layer is in the midst of its transitional state (see figure 27), and where there are large wall-normal velocity gradients in the region connecting the inner and outer parts of the boundary layer. The over-shoot decreases further downstream as the flow becomes fully turbulent. At the exit $x = 3.5$ ($Re_\theta = 1120$) the computed mean velocity profile $\overline{u}/U_{\text{ref}}$ is in excellent agreement with the experimental data of Webster *et al.* Figure 22($c$) plots $\overline{u}/U_{\text{ref}}$ with respect to $y$ to show the absolute change. Away from the wall the variation with streamwise distance is monotonic, corresponding to the growth of the boundary layer shown in figure 20. The inner part drops from $x = 0.5$ to 1.0 first, before $\overline{u}$ starts to increase. This is entirely consistent with the skin friction variation shown in figure 21.

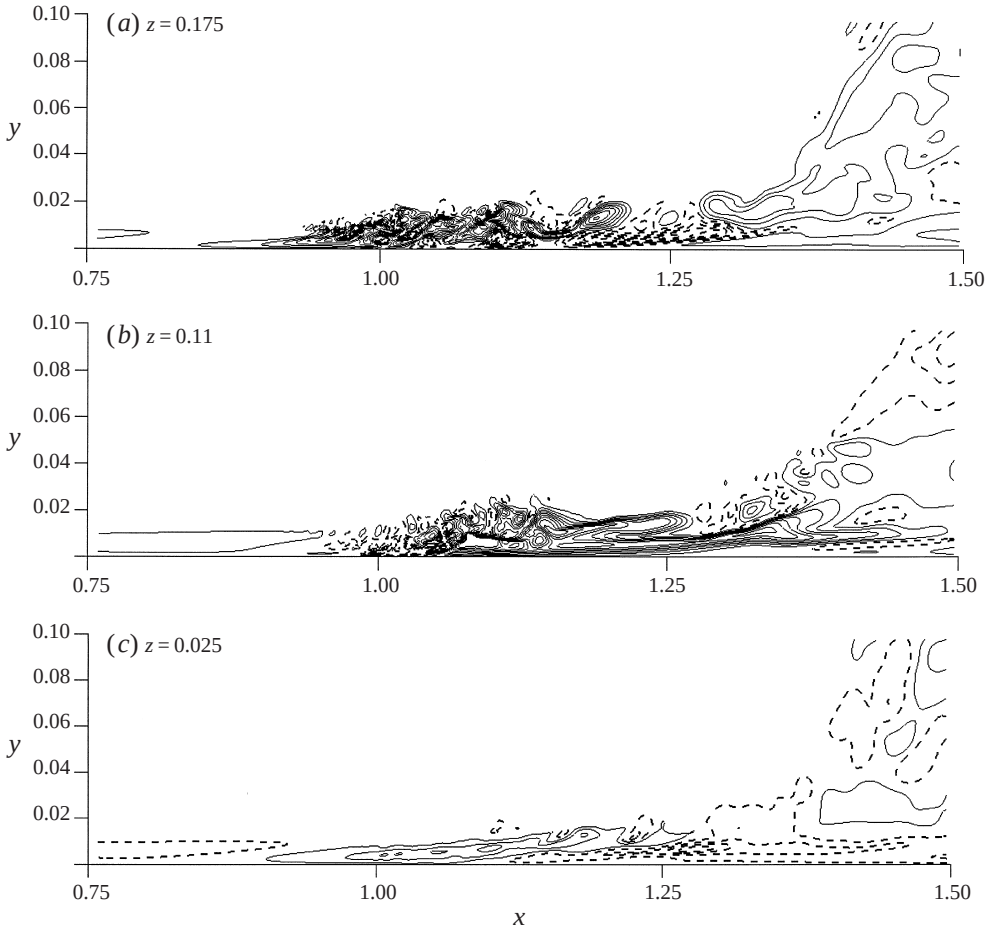


FIGURE 19. Visualization of the forcing by free-stream eddies through localized instability using $u'$ over three $(x, y)$-planes at $t/\mathscr{T}=33.6$; $0.02U_{\text{ref}} \leqslant |u'| \leqslant 0.34U_{\text{ref}}$ with increment 0.04.

Time-averaged turbulence intensities and Reynolds shear stress at six streamwise stations are presented in figure 23, together with the DNS data of Spalart (1988) obtained from a turbulent flat-plate boundary layer at $Re_\theta = 1410$. Figure 23(*a*) shows that even at the early stage of transition $x = 0.5$ there exist relatively large streamwise fluctuations in the outer part of the boundary layer, but the levels of wall-normal intensity and Reynolds shear stress are very low. This is consistent with previous studies discussed by Alfredsson & Matsubara where streamwise intensity was found to have a maximum in the centre of the boundary layer. At $x = 1.0$ and 1.5 the profiles of $\overline{\langle u'^2 \rangle}^{1/2,+}$ exhibit large over-shoots in the outer region compared to the fully turbulent profile. Significantly the peaks are also located away from the wall, e.g. $0.15\delta$ for $x = 1.0$. Unlike the three turbulence intensities, Reynolds shear stress increases from $x = 0.5$ to 1.5 almost monotonically throughout the boundary layer and asymptotes to that of Spalart (1988). Note, however, that all the profiles shown in figure 23 are normalized by the local friction velocity, which masks the absolute changes between different streamwise stations (see figure 25). Figure 23(*e*) shows that at $x = 2.5$, after the end of transition, profiles of turbulence intensities and Reynolds

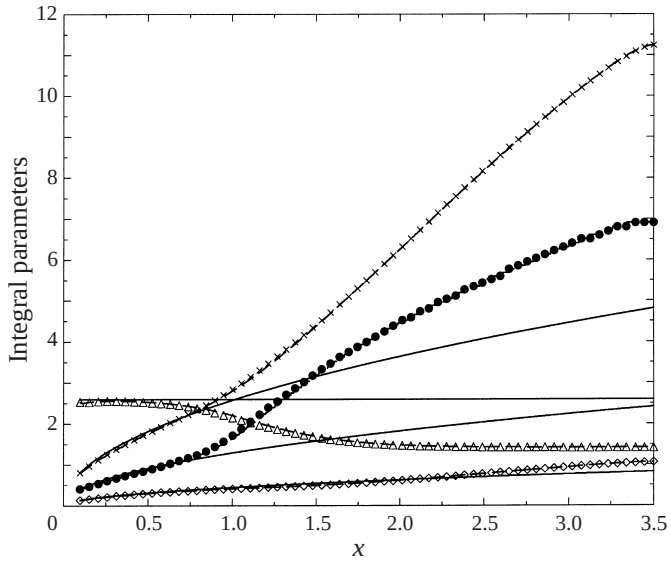


FIGURE 20. Time-averaged mean boundary layer integral parameters: ——, Blasius solution without wake; — —, simulation with $\Delta z^+_{x=3} = 11$ ($\Delta z^+_{x=1} = 8.4$); symbols, simulation with $\Delta z^+_{x=3} = 8.25$ ($\Delta z^+_{x=1} = 6.3$): ●, $10^2\delta$; ◇, $10^2\delta^*$; △, $\delta^*/\theta$; ×, $10^{-2}Re_\theta$.

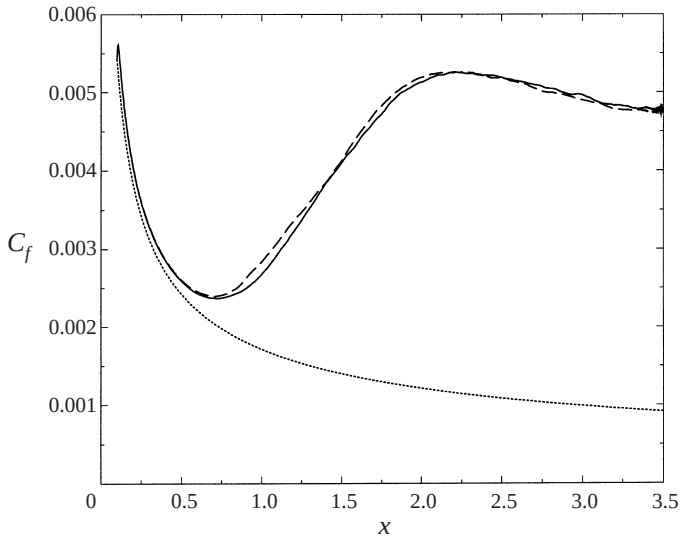


FIGURE 21. Time-averaged mean skin-friction coefficient: ·····, Blasius solution without wake; ——, simulation with $\Delta z^+_{x=3} = 11$ ($\Delta z^+_{x=1} = 8.4$); — —, simulation with $\Delta z^+_{x=3} = 8.25$ ($\Delta z^+_{x=1} = 6.3$).

shear stress are in very good agreement with Spalart's DNS. As expected, the free-stream intensities are higher than Spalart (1988) because of the passing wake. From $x = 2.5$ on downstream, changes in the profiles are minimal. At the exit (figure 23*f*) the maximum value of $\overline{\langle u'^2 \rangle}^{1/2,+}$ and its location are in excellent agreement with Spalart (1988). The profile also develops a shoulder near $0.15\delta$ which is commonly found in low Reynolds number boundary layer flows.

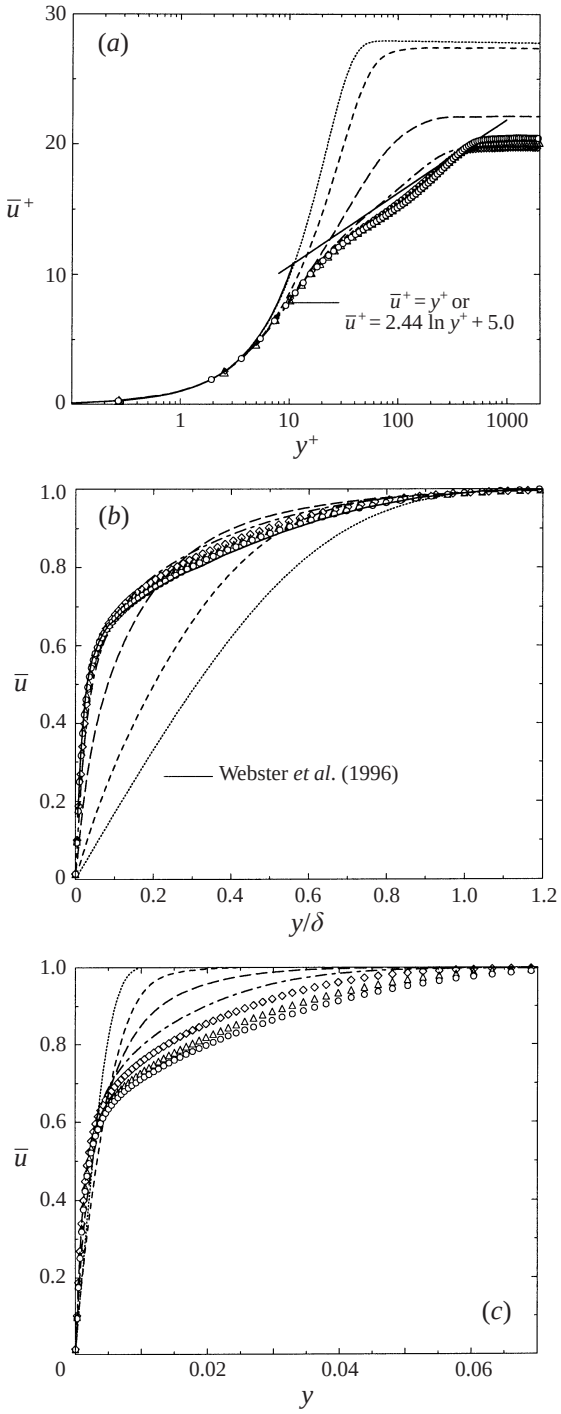


FIGURE 22. Time-averaged mean streamwise velocity: ·····, $x = 0.5$; – – –, $x = 1.0$; ——, $x = 1.5$; —·—, $x = 2.0$; ◇, $x = 2.5$; △, $x = 3.0$; ○, $x = 3.5$ (exit).

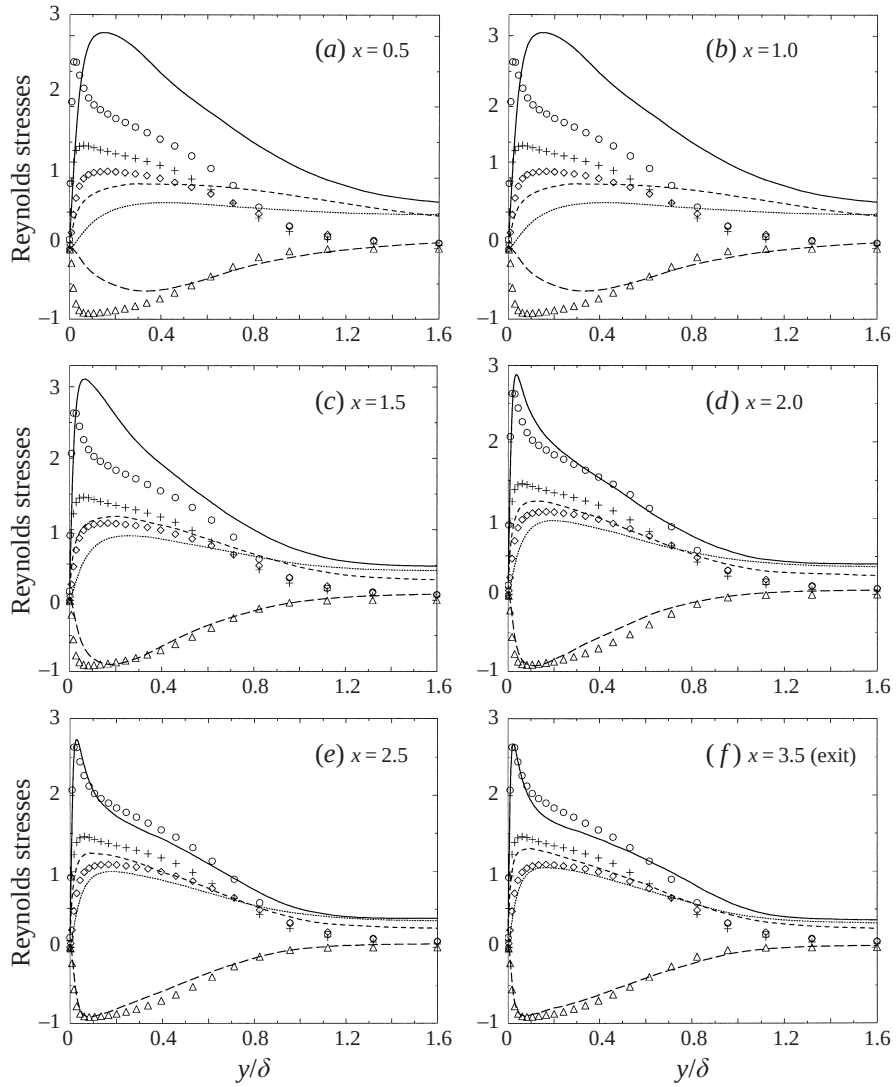


FIGURE 23. Time-averaged Reynolds stresses in outer coordinates; ——, $\overline{\langle u'^2\rangle}^{1/2,+}$; ·····, $\overline{\langle v'^2\rangle}^{1/2,+}$; – – – –, $\overline{\langle w'^2\rangle}^{1/2,+}$; — —, $\overline{\langle u'v'\rangle}^{+}$; symbols: flat-plate boundary layer of Spalart (1988) at $Re_\theta = 1410$.

Profiles of the time-averaged and normalized (on wall parameters) turbulence kinetic energy production rate $\mathscr{P}^+ = -\overline{\langle u'v'\rangle}^{+}\,\partial\overline{u}^+/\partial y^+$ at eight streamwise stations are compared to the DNS of Spalart (1988) and the experimental data of Kim, Kline & Reynolds (1968) in figure 24. Spalart noticed that his DNS profiles of $\mathscr{P}^+$ at three different momentum thickness Reynolds numbers are self-similar and also agree very well with Kim *et al.* He attributed this to the fact that at such relatively low Reynolds numbers the decrease of Reynolds shear stress and the increase of mean velocity gradient cancel each other in the product to a remarkable degree. It is clear from figure 24 that the present computation faithfully reproduces this feature, as evident in the self-similarity of the profiles at $x = 2.5$, 3.0 and 3.5 and the agreement with Spalart (1988) and Kim *et al.* (1968).

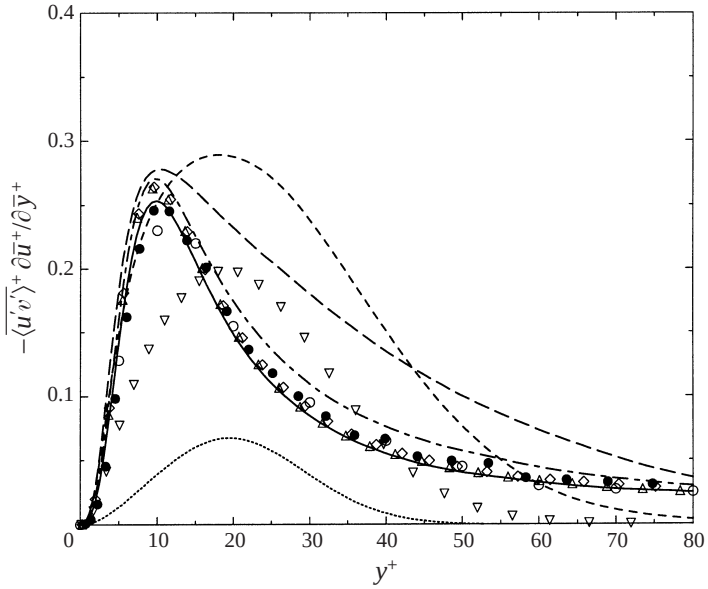


FIGURE 24. Time-averaged non-dimensional turbulence kinetic energy production near the wall: ●, Spalart (1988); ○, Kim, Kline & Reynolds (1968); ·····, $x = 0.5$; ▽, $x = 0.75$; – – – –, $x = 1.0$; ——, $x = 1.5$; —·–, $x = 2.0$; ◇, $x = 2.5$; △, $x = 3.0$; ——, $x = 3.5$ (exit).

In the transition region the peak of $\mathscr{P}^+$ is located away from the wall and there is also a large over-shoot. This is consistent with the turbulence intensity and Reynolds shear stress profiles presented in figure 23. As the flow approaches the end of transition, the peak shifts towards the wall and the maximum value of $\mathscr{P}^+$ drops. Again, note that the profiles are normalized by the local friction velocity. A clearer picture of the streamwise evolution of the absolute peak values is given in figure 25. This figure shows local maxima of time-averaged turbulence kinetic energy, wall-normal fluctuations, Reynolds shear stress and turbulence kinetic energy production. A large over-shoot in turbulence kinetic energy is seen prior to the completion of transition. The peak is located at $x \approx 1.85$. The time-averaged wall-normal fluctuations do not show as noticeable an over-shoot as the turbulence kinetic energy. Production of turbulence kinetic energy and Reynolds shear stress peak at the same location, though the degree of over-shoot is much stronger for the former. The location where the Reynolds shear stress attains its maximum value is the same as the time-averaged mean skin friction, i.e. $x \approx 2.15$. In the time-averaged sense this also corresponds to the end of transition as indicated by the results shown in figures 22, 23 and 24.

Overall, the results presented in this section demonstrate that the present simulations yield correct time-averaged flow statistical properties in the laminar regime near the inlet and the fully turbulent regime near the exit. Between these two ends time-averaged mean and second-order statistics profiles across the boundary layer seldom vary monotonically with the increase of $x$. Completion of transition, in a time-averaged sense, can be defined as where the mean skin friction reaches its peak value. At this location ($Re_\theta \approx 660$) Reynolds shear stress and production of turbulence kinetic energy also attain their peak values. Downstream profiles of the mean and turbulence statistics are in good agreement with previous DNS and experimental data for fully turbulent flat-plate boundary layers. In the work

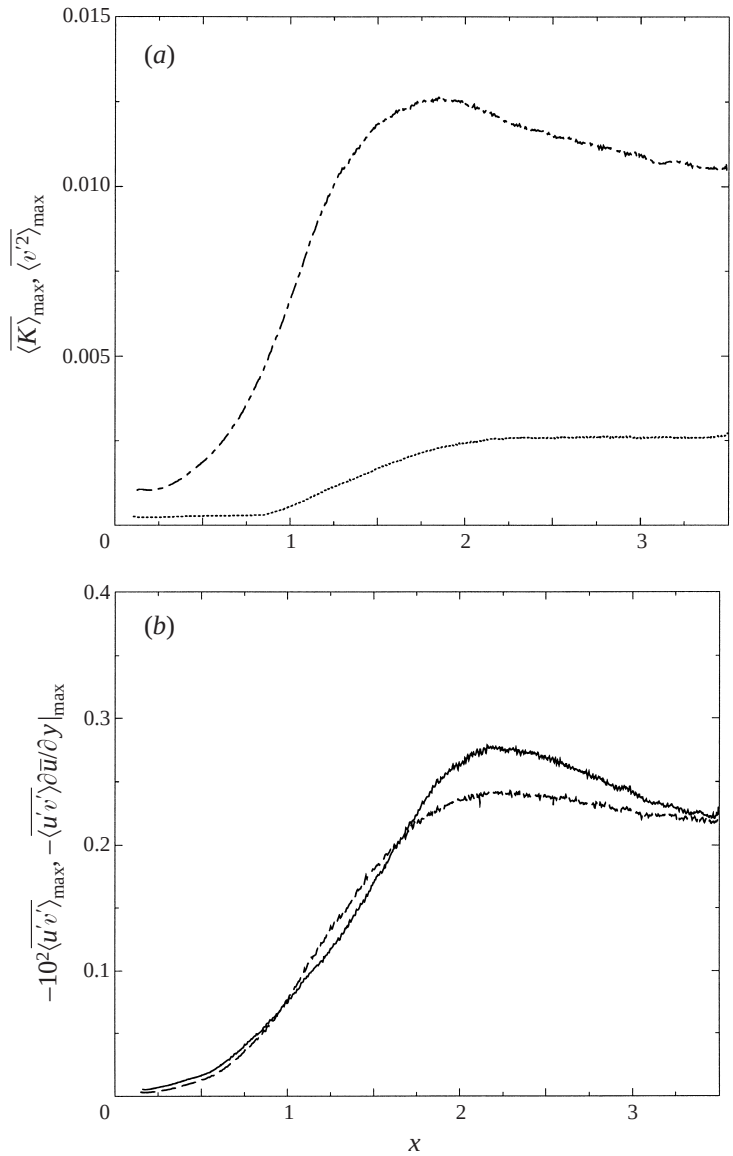


FIGURE 25. Streamwise evolution of maximum Reynolds stresses: — - –, turbulence kinetic energy; ·····, wall-normal fluctuation; — —, shear stress; ——, production of turbulence kinetic energy.

of Liu & Rodi (1991), the location of transition was considered to be where the turbulent strips merge, and where the turbulence intensity reaches the level prevailing in turbulent boundary layers. The location of merging is difficult to define, since it involves transient behaviour and many other subjective factors. Turbulence intensities also develop over-shoot characteristics in the process of transition. At the given passing frequency their estimated transition location is $x \sim 1.85$. Taking into account the different definitions, there is an overall agreement in the transition location between the present computation and the experiments of Liu & Rodi (1991).

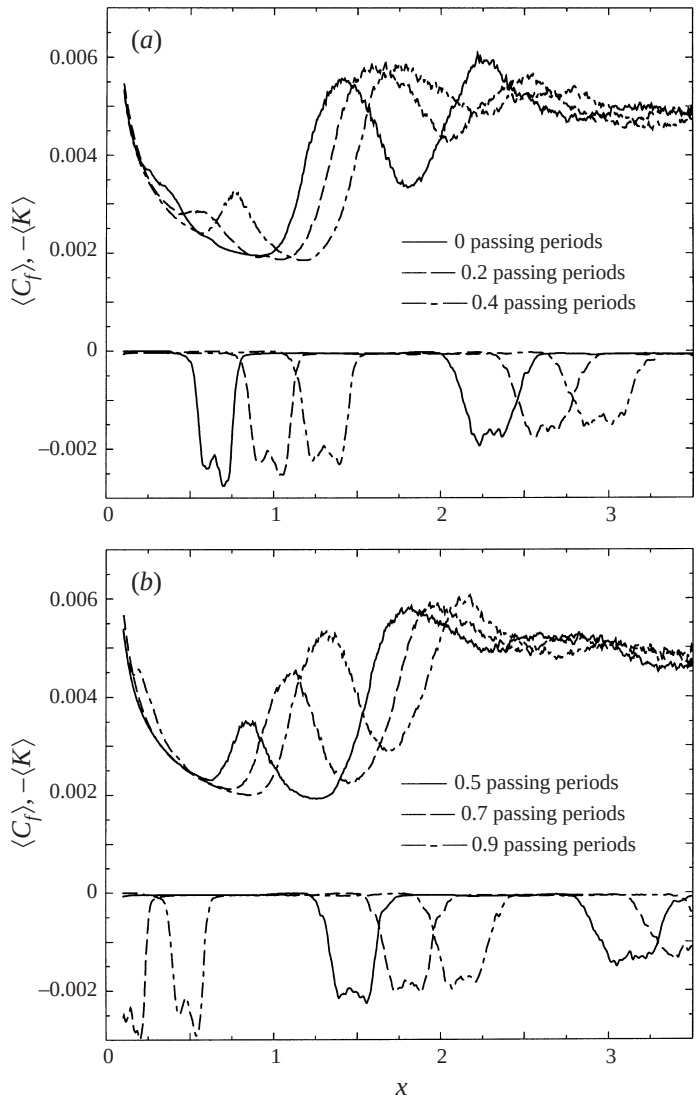


FIGURE 26. Streamwise distributions of phase-averaged skin-friction coefficient and free-stream turbulence kinetic energy; upper curves: $\langle C_f \rangle$; lower curves: $-\langle K \rangle$ at $y = 0.1$.

## 6. Phase-averaged boundary layer properties

Time averaging is not equivalent to ensemble averaging in this non-stationary flow. The phase average gives a fuller statistical picture. At $t_{n_{\mathcal{T}}} = 0.9$ and 0 the wake is completely outside the (computational) inflow plane. At these two instants the velocity profiles simply follow the Blasius solution. Beginning from $t_{n_{\mathcal{T}}} = 0$ the wake starts to enter from the top boundary of the inflow plane and descends towards the flat plate. Touch-down occurs slightly before $t_{n_{\mathcal{T}}} = 0.7$. Streamwise variations of the phase-averaged skin friction and turbulence kinetic energy in the free stream (at $y = 0.1$) are shown in figure 26. As the wake passes along the plate its strength is attenuated, which is also accompanied by a spread in wake width. This effect is seen in the $K$ versus $x$ plots. The $\langle C_f \rangle$ versus $x$ plot shows a local rise in the laminar region

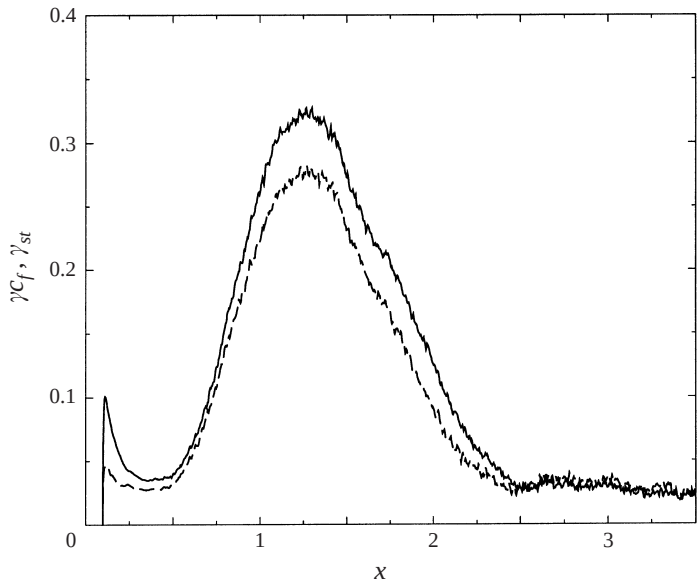


FIGURE 27. Streamwise profiles of the parameter $\gamma$ indicating boundary layer transitional state: ——, based on r.m.s. periodic skin-friction fluctuation; — —, based on r.m.s. periodic Stanton number fluctuation.

when the wake buffets the layer. This is distinct from the larger, sustained rise further downstream where transition occurs, and the boundary layer becomes fully turbulent. The location of the rise lags the free-stream wake passage as previously discussed. After the completion of transition no distinct peaks can be seen in the phase-averaged r.m.s. skin-friction fluctuations even though the turbulent layer is still buffeted by the wake. Over the distance where the rise is observed there is a change in the nature of the fluctuations that occurs at around 0.4 passing periods, when the wake reaches $x \approx 0.7$. At that point, turbulent spots begin to appear and the fluctuation profiles peak deeper in the boundary layer. The appearance changes from that of a buffeted layer to one with self-sustained turbulence. Similar features have also been reported by Halstead *et al.* (1997) in multi-stage compressor/turbine measurements.

Figure 27 shows the streamwise distribution of the r.m.s. periodic skin-friction fluctuation coefficient $\gamma_{C_f}$ defined as

$$\gamma_{C_f} = \left\{ \overline{\left( \langle C_f \rangle - \overline{C}_f \right)^2} \right\}^{1/2} / \overline{C}_f. \tag{8}$$

This coefficient is a good indicator for the boundary layer's transitional state. Also presented in the figure is the streamwise distribution of the r.m.s. periodic Stanton number fluctuation coefficient $\gamma_{St}$, obtained from a heat transfer simulation in which the wall was slightly heated (Wu & Durbin 1999*a*). In a laminar flow $\gamma_{C_f} = 0$; after completion of transition in a fully turbulent flow $\gamma_{C_f} \to 0$ if the sample size is sufficiently large. The definition of $\gamma_{C_f}$ is precise and does not involve arbitrarily chosen threshold values. The spike at the inlet station is due to impact of the passing wake on the flat plate. The small peak quickly decays and reaches a local minimum at $x \approx 0.3$. The transitional state of the boundary layer at this location is the lowest prior to the completion of transition. This is again consistent with the notion that turbulence directly carried by the wake into the near-wall region decays rapidly. $\gamma_{C_f}$ reaches its global maximum at $x \approx 1.2$, indicating that at this station the boundary

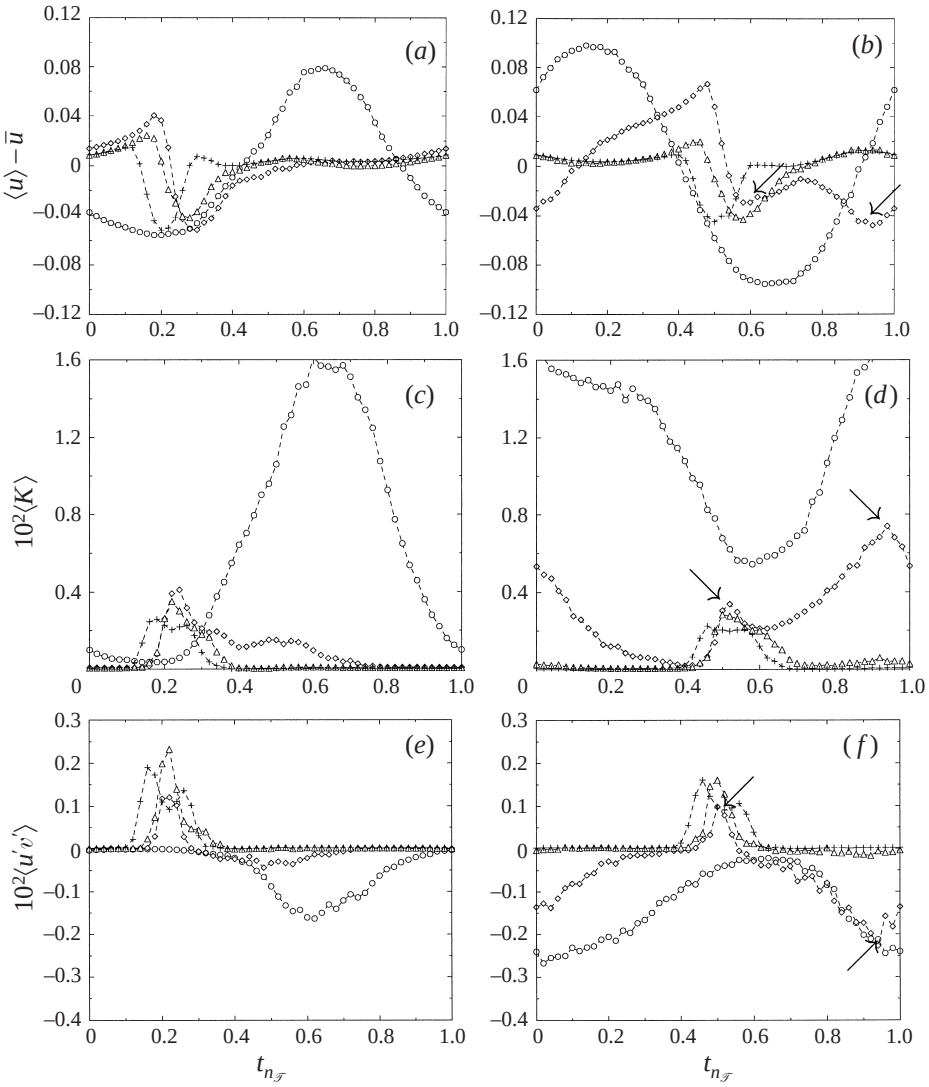


FIGURE 28. Periodic fluctuation of streamwise velocity, phase-averaged turbulence kinetic energy and Reynolds shear stress: ○, $y = 0.002$; ◇, $y = 0.02$; △, $y = 0.04$; +, $y = 0.1$; $(a, c, e)$ $x = 1.0$; $(b, d, f)$ $x = 1.5$.

layer has the strongest transitional state, in the sense that the properties of the boundary layer are most distant from those in either the laminar or turbulent regime. Figure 27 also shows that within the transition region the degree of upstream and downstream asymmetry of $\gamma_{C_f}$ with respect to its peak location is relatively small.

In the remainder of this section we focus on space–time characteristics of the phase-averaged mean velocity and second-order turbulence statistics in the transitional region. Figure 28$(a, b)$ presents the periodic streamwise velocity fluctuation $\langle u\rangle - \overline{u}$ at $x = 1.0$ and 1.5 as a function of phase $t_{n_{\mathcal{F}}}$. At each streamwise station four profiles are shown which are taken from $y = 0.002$, 0.02, 0.04 and 0.1. Figures 28$(c, d)$ and figure 28$(e, f)$ present profiles of the phase-averaged turbulence kinetic energy $\langle K\rangle$ and turbulent shear stress $\langle u'v'\rangle$ at the same locations, respectively.

The highest wall-normal location $y = 0.1$ in the figure remains outside the time-averaged boundary layer at both streamwise stations. The variations obtained at $y = 0.1$ then simply reflect, for the most part, the free-stream wake passing. Profiles of $\langle u \rangle - \overline{u}$ at the most inner wall-normal location $y = 0.002$ display sine wave behaviour. The amplitude of the sine wave motion is strongest when the flow has the largest $\gamma_{C_f}$, and decreases towards zero in laminar and fully turbulent regions. The peak in the sine wave has a phase lag behind the free-stream wake. The variation of $\langle K \rangle$ at $y = 0.002$ shows the statistically averaged effect of turbulent spots. Since at $x = 1.0$ transition is still in the early stage, $\langle K \rangle$ and $\langle u'v' \rangle$ in figure 28($c, e$) return to zero after the statistically averaged effect of turbulent spots has passed. This is different from the situations shown in figure 28($d, f$) where turbulence fluctuations do not return to zero for the whole period because transition is already at its late stage. In the fully turbulent region $\langle u \rangle - \overline{u}$, $\langle K \rangle$ and $\langle u'v' \rangle$ inside the boundary layer approach their time-averaged mean with little sign of phase dependence. Note that the shear stress inside the free-stream wake is positive. This is a consequence of the wake orientation.

In the transitional region, the behaviour of $\langle u \rangle - \overline{u}$ in the central part of the boundary layer obtained from $y = 0.02$ is interesting. Figure 28($b$) shows the profile has two dips within one passing period. These two dips correspond to the two peaks of $\langle K \rangle$ at the same wall-normal location shown in figure 28($d$). The peak of $\langle K \rangle$ between $t_{n_{\mathcal{F}}} \approx 0.5$ and 0.6 is clearly from the free-stream passing wake, and the other one between $t_{n_{\mathcal{F}}} \approx 0.9$ and 1.0 is from the statistically averaged effect of turbulent spots. Thus the early dip in $\langle u \rangle - \overline{u}$ is from the wake deficit, and the late dip is because of the temporal thickening of boundary layer arising from the statistically averaged effect of turbulent spots. These dips do not appear before the onset, or after the end, of transition. Liu & Rodi (1991) also discussed similar dips in their experimental results. They offered two possible explanations, the first being that upward cylinder motion at the far end of the rotating disk caused secondary wakes and the second being that near-wall turbulent spots cause temporal thickening of boundary layer. Our results demonstrate that the latter is the major cause.

## 7. Additional simulations and thought experiments

### 7.1. *Effect of periodic velocity fluctuation on transition*

The experimental measurements of Orth (1993) suggest that periodic velocity fluctuations caused by the passing wake have negligible effect on transition. Our thought experiment presented in this subsection supports his conclusion.

Additional DNS simulations were performed on two hypothetical flows. In the first, the wake turbulence was discarded and only the mean profiles were fed into the flow domain. No turbulent fluctuations occurred over the computational region. A phase-averaged mean flow perturbation was seen immediately beneath the wake, but this was localized and did not lead to instability (which could only be induced by numerics). A comparison between the phase-averaged velocity distortions under the zero and normal turbulence wakes is made in figure 29. The boundary layer lies below $y = 0.0076$. A weak inflection of the instantaneous boundary layer profile was noticed in the zero intensity case. This transient inflection was insufficient to produce breakdown to turbulence inside the boundary layer (in the case when low level turbulence was added to the wake).

In the second additional simulation the wake turbulence was reduced to 1% of

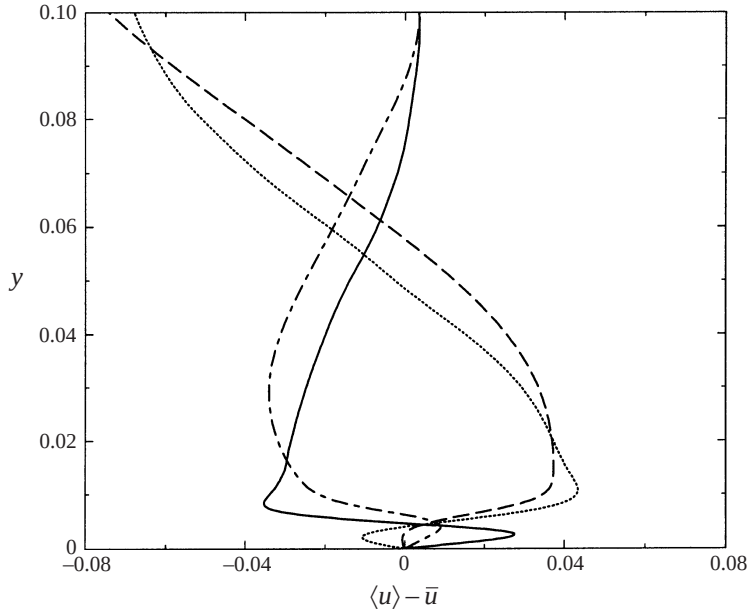


FIGURE 29. Periodic velocity fluctuation profiles at $x = 0.5$ in the baseline simulation with full wake turbulence and in the additional simulation where the inlet wake turbulence is reduced to zero. Full wake turbulence ($\delta = 0.0086$): ——, $t_{n_{\mathscr{T}}} = 0.9$; · · · · ·, $t_{n_{\mathscr{T}}} = 0.05$. Zero wake turbulence ($\delta = 0.0076$): — —, $t_{n_{\mathscr{T}}} = 0.9$; — - –, $t_{n_{\mathscr{T}}} = 0.05$.

its natural level. Figure 30(*a*) presents contours of instantaneous streamwise velocity, $u - U_{\text{ref}}$ over an $(x, y)$-plane at $t/\mathscr{T} = 8.0$. The velocity contours show no sign of turbulent spots or of transition. Figure 30(*b*) presents contours of $u'$ over the $(x, z)$-plane at $y/L = 7.38 \times 10^{-4}$ at the same instant. The near-wall disturbances generated at the inlet evolve toward long-streamwise-wavelength waves, with spanwise modulation. The wake passage is seen more clearly in the $v'$ profiles of figure 30(*c*). These figures show that the boundary layer filters out short-wave inlet disturbances (Jacobs & Durbin 1998). They decay rapidly and are not the origin of the small-scale spots that occur beneath higher free-stream wake turbulence.

### 7.2. *Effect of streamwise pressure gradient on transition*

Streamwise pressure gradient exerts an overwhelming influence on the stability of a laminar boundary layer. A decrease in pressure in the downstream direction, i.e. favourable gradient, has a stabilizing effect. In the case of a flat plate this causes the critical Reynolds number to become larger than $Re_\theta = 200$. An adverse gradient leads to instability.

The manner in which the wakes are introduced at the inlet causes a localized streamwise pressure gradient. The inlet velocity distribution is a superposition of Blasius and wake velocity profiles. This distribution is forced to satisfy the no-slip boundary condition at the inflow station by an artificial damping through the use of (7).

It has been suggested in the literature that passing wakes produce streamwise pressure gradients of opposite sign depending upon the sign of $U_{\text{cyl}}$ (see figure 2). Hodson (1985) and Hodson & Dawes (1998) discussed a 'negative jet' concept related to this subject. They argued that a negative vertical velocity component inside the

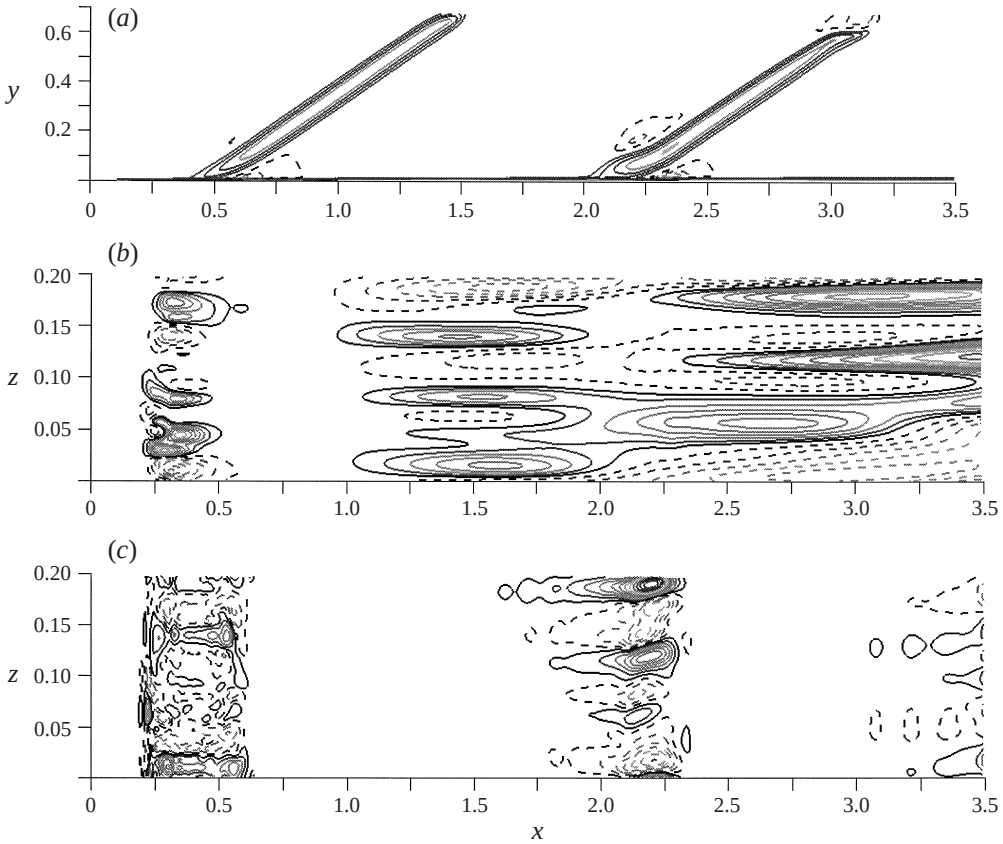


FIGURE 30. Instantaneous velocity fields at $t/\mathscr{T} = 8.0$ in the additional simulation where the inlet wake turbulence is reduced by a factor of 100: (*a*) $u - U_{\mathrm{ref}}$ over one $(x, y)$-plane; (*b*) $10^2 u'$ over the $(x, z)$-plane of $y = 7.38 \times 10^{-4}$; (*c*) $10^2 v'$ over the $(x, z)$-plane of $y = 7.38 \times 10^{-4}$.

wake causes a high-pressure stagnation point on the wall. Thus there exists a localized favourable pressure gradient near the wake. When $U_{\mathrm{cyl}}$ is positive instead of negative, they argued that the positive vertical velocity component inside the wake results in a low-pressure point on the wall, causing a localized adverse pressure gradient near the wake. However, Hunt, Durbin & Wu (1998) have shown that the pressure change associated with this 'negative jet' effect is quite small since its magnitude is dependent to the square of the wake velocity deficit. Nevertheless, the reasoning of Hodson (1985) may still be helpful in understanding the inlet pressure gradient encountered in the current study.

At the inlet, when $U_{\mathrm{cyl}} < 0$ the mass contained inside the 'negative jet' is forced to enter the computational domain as the wall is approached because the wake deficit is damped by Blasius to satisfy no slip. This results in a localized high pressure. When $U_{\mathrm{cyl}} > 0$ the mass contained inside the 'negative jet' is sucked away from the computational domain as the wall is approached, thus producing a localized low pressure at the wall. We will present three additional numerical experiments in this subsection to demonstrate and quantify the effect of inlet streamwise pressure gradient on wake-induced boundary layer transition.

Pictures of the three boundary layers, drawn using contours of the instantaneous streamwise velocity $u$ over one random $x, y$ cross-section, are shown in figure 31.

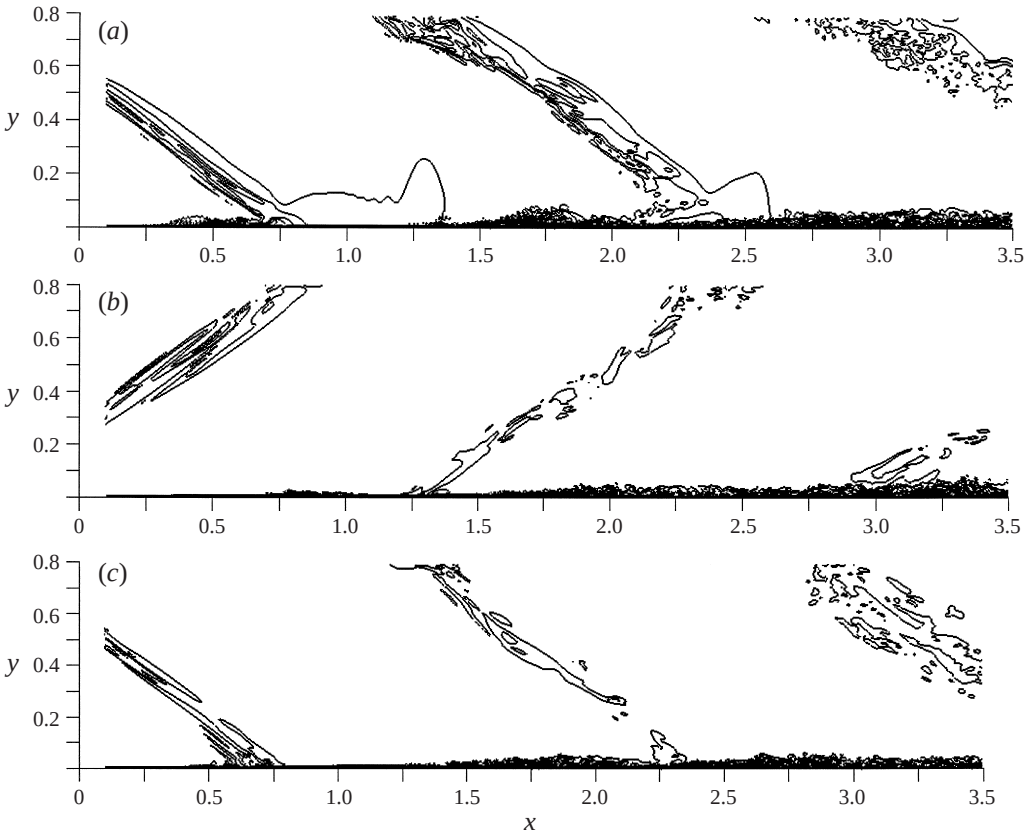


FIGURE 31. Instantaneous velocity $u$ over one $(x, y)$-plane: (*a*) additional simulation with $U_{\text{cyl}} = +0.7U_{\text{ref}}$; (*b*) additional thought experiment with inlet mean wake deficit set to zero ($U_{\text{cyl}} = -0.7$); (*c*) additional thought experiment with inlet mean wake deficit set to zero ($U_{\text{cyl}} = +0.7$).

Figure 31(*a*) corresponds to a simulation in which $U_{\text{cyl}} = +0.7U_{\text{ref}}$ as opposed to $-0.7U_{\text{ref}}$ in the baseline case. Figure 31(*b*) and figure 31(*c*) correspond to two thought experiments with inlet mean wake deficit being set to zero and $U_{\text{cyl}} = \pm 0.7$, respectively. The inlet wakes in figures 31(*b*) and 31(*c*) are therefore of shear-free type, i.e. mean wake velocities $\langle u_{\text{wake}} \rangle_z$ and $\langle v_{\text{wake}} \rangle_z$ have been subtracted from the corresponding inlet wake profiles while retaining only the turbulence fluctuations.

Figure 32 shows the time-averaged streamwise pressure coefficient in the three cases, together with that in the baseline case. $C_{pw}$ is defined as $2(\overline{p}_{\text{wall}} - \overline{p}_{\text{wall, inlet}})/U_{\text{ref}}^2$. It is seen from figure 32 that when inlet mean wake deficit is retained, damping using Blasius of the downward-moving wake results in a mild favourable pressure gradient in the region $x < 0.75$. Damping using Blasius of the upward-moving wake produces a mild adverse pressure gradient in the same region. Also evident from figure 32 is that a nearly zero streamwise pressure gradient is achieved beyond $x = 0.75$ for all the cases, except for near the exit where a slight favourable pressure gradient is visible. Streamwise pressure gradients in both of the shear-free wake cases are nearly identical and essentially zero across the whole computational domain. Without a mean wake

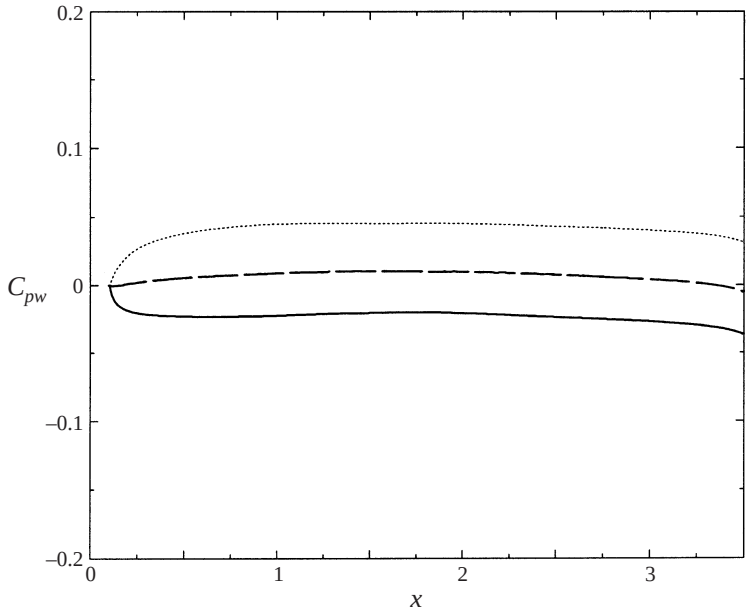


FIGURE 32. Time-averaged wall static pressure coefficient: ——, baseline case $U_{\text{cyl}} = -0.7$; ·····, additional simulation $U_{\text{cyl}} = +0.7$; – – –, additional simulation with inlet mean wake deficit set to zero ($U_{\text{cyl}} = -0.7$); ——, additional simulation with inlet mean wake deficit set to zero ($U_{\text{cyl}} = +0.7$).

deficit, the no-slip condition forced at the inlet by Blasius damping results in minimal distortion of the flow.

Figure 33 compares visualizations of the boundary layer transition processes. Shown in the figure are contours of instantaneous wall-normal velocity fluctuation $v'$ over the $(x, z)$-plane of $y = 7.38 \times 10^{-4}$. Fluctuations with magnitude smaller than 0.005 are grouped into the background. Figure 33($a$) shows that under a mild localized adverse pressure gradient, wake turbulence introduced from the inlet does not exhibit rapid decay in the near-wall region. A quasi-two-dimensional turbulent strip forms right from the inlet. No isolated turbulent spots emerge in this instance. At the instant shown on figure 33($a$), three turbulent regions co-exist and are separated streamwise by relatively 'quiet' laminar-like strips. In the baseline case only two streamwise separated turbulent regions co-exist at any time despite the fact that the passing frequency $\mathscr{T}$ is the same in both cases.

Figures 33($b$) and 33($c$) visualize the boundary layer transition processes for the two shear-free wake cases. The emergence of turbulent spots occurs closer to the inlet than in the baseline case. For both of the shear-free wake cases there are two full turbulent strips plus isolated turbulent spots over the entire $(x, z)$-plane. Thus elimination of the streamwise pressure gradients makes the transition processes nearly the same, regardless of the wake orientation. Such a characteristic is also manifested in statistically averaged boundary layer properties. Figure 34 shows the time-averaged skin-friction coefficient for all the four cases. A localized favourable pressure gradient delays the minimal skin-friction location but with a higher over-shoot. A localized adverse pressure gradient makes the minimal skin friction occur closer to the inlet but with a lower $C_f$ in the turbulent region. Removing the mean wake deficit produces an intermediate skin-friction distribution.

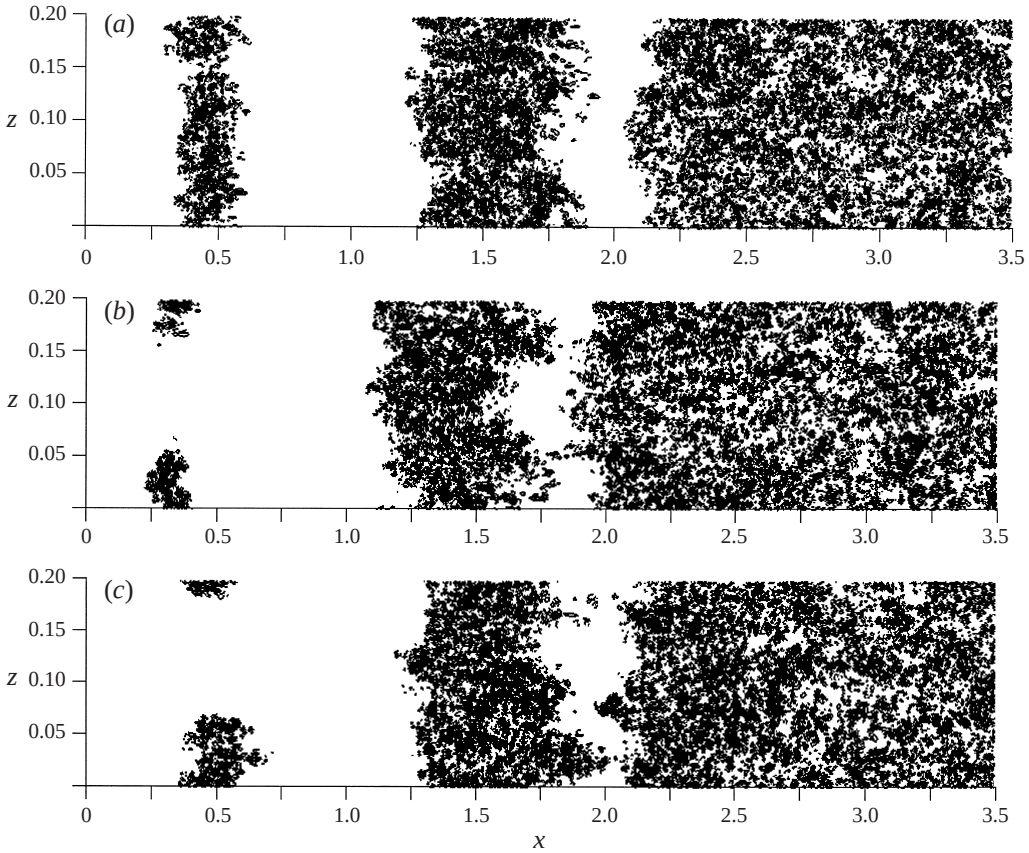


FIGURE 33. Instantaneous wall-normal fluctuation $v'$ over the $(x, z)$-plane of $y = 7.38 \times 10^{-4}$: (*a*) additional simulation with $U_{\text{cyl}} = +0.7U_{\text{ref}}$; (*b*) additional thought experiment with inlet mean wake deficit set to zero ($U_{\text{cyl}} = -0.7$); (*c*) additional thought experiment with inlet mean wake deficit set to zero ($U_{\text{cyl}} = +0.7$).

## 8. Summary

A notable feature of the present study is its dual relevance to the fundamental subject of boundary layer instability under moderate levels of disturbance, and the engineering subject of turbomachinery aerodynamics.

The concept of puffs has proven to be relevant in passing wake-induced bypass transition. Such structures evolve from near-wall leading-edge (inlet) disturbances through a receptivity phase. They have a tendency to elongate and decay. Amplification is observed when certain types of free-stream vortices interact with the boundary layer flow through a local Kelvin–Helmholtz-like instability. Breakdown in wake-induced bypass transition usually occurs in the outer part of the boundary layer, following the typical Kelvin–Helmholtz-type wavy motion in the velocity field. When this happens, negative streamwise fluctuations associated with the inflectional profiles evolve into strong forward eddying motions, producing young turbulent spots. Violent upward motion exists near the interface of the positive/negative streamwise fluctuations. This interface also forms the downstream edge of the turbulent spot. Thought experiments show mean wake distortion of the boundary layer is less important in receptivity and transition compared to the interaction between boundary layer and free-stream

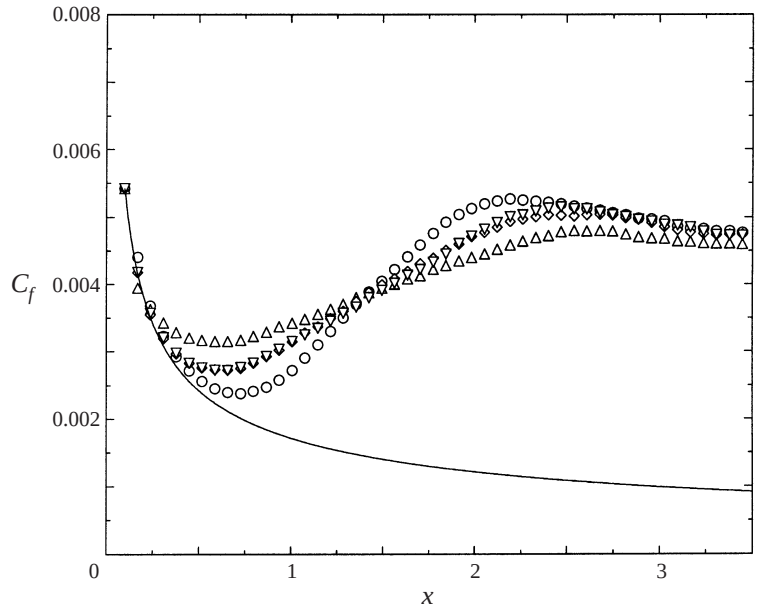


FIGURE 34. Time-averaged skin-friction coefficient: ○, baseline case $U_{\rm cyl} = -0.7$; △, additional simulation $U_{\rm cyl} = +0.7$; ◇, additional simulation with inlet mean wake deficit set to zero ($U_{\rm cyl} = -0.7$); ▽, additional simulation with inlet mean wake deficit set to zero ($U_{\rm cyl} = +0.7$); ——, Blasius solution without wake; every other 20 points are shown.

turbulent eddies carried by the passing wakes. These findings have answered, to a satisfactory degree, all the questions we have raised in § 1.

Visualizations obtained from this study have been compared to the liquid crystal experiments of Zhong *et al.* (1998) and Kittichaikaran *et al.* (1999). Specifically, geometrical characteristics of the simulated and measured puffs prior to breakdown, as well as the matured turbulent spot, are found to be in good agreement. The turbulent spot has an arrowhead pointing upstream, in the reverse direction to many previous fundamental studies on boundary layer instability. We discovered that when breakdown occurs in the outer layer, where the local convection speed is large, as in the present case, the arrowhead points upstream. This often happens when the boundary layer is subjected to perturbation by free-stream eddies. When breakdown occurs near the wall, e.g. as a result of a disturbance artificially introduced at the wall, the turbulent spot has an arrowhead pointing downstream.

We have also studied the wake-induced transition problem from a statistical point of view. The computed boundary layer properties upstream of the onset of transition follow the Blasius solution, and those after the completion of transition follow fully developed canonical turbulent boundary layers. During transition the peak of turbulence kinetic energy is displaced away from the wall, in agreement with Alfredsson & Matsubara (1996). Completion of transition is marked by the streamwise location where the time-averaged mean skin friction reaches its maximum. Reynolds shear stress and production of turbulence kinetic energy also attain their maxima at the same location, while turbulence kinetic energy peaks further upstream. During transition phase-averaged mean streamwise velocity in the near-wall region displays sinusoidal behaviour in time. The amplitude of such sine wave motion peaks when the boundary layer is most distant from both laminar and turbulent regimes. In

the central part of the boundary layer, the phase-averaged mean streamwise velocity exhibits two dips for each passing cycle, one from the passing wake deficit, the other from the statistically averaged effect of turbulent spot growth. These features are in agreement with the experiments of Liu & Rodi (1991). Unsteady Reynolds-averaged Navier–Stokes (RANS) computations of this wake-induced transitional boundary layer have also been conducted, and the predictions compared with present DNS data. That work was reported in Wu & Durbin (1998, 1999*a*, *b*).

We thank Charles D. Pierce for the use of his code. This work is supported by the Academic Strategic Alliance Program of the US Department of Energy Accelerated Strategic Computing Initiative. The simulations were performed on the Cray T3E at the Pittsburgh Supercomputing Center (PSC). Discussions with D. S. Henningson, H. P. Hodson, S. K. Lele, P. Moin, W. C. Reynolds and M. M. Rogers are gratefully acknowledged. The computer hardware support from M. Fatica and R. Subramanya (PSC) is gratefully acknowledged. J.C.R.H. is grateful to the Center for Turbulence Research for support during this work.

## REFERENCES

Addison, J. S. & Hodson, H. P. 1990 Unsteady transition in an axial flow turbine, part 1: measurements on the turbine rotor; part 2: cascade measurements and modeling. *Trans. ASME: J. Turbomachinery* **112**, 206–214.

Akselvoll, K. & Moin, P. 1996 Large eddy simulation of turbulent confined coannular jets. *J. Fluid Mech.* **315**, 387–411.

Alfredsson, P. H. & Matsubara, M. 1996 Streaky structures in transition. In *Transitional Boundary Layers in Aeronautics* (ed. R. A. W. M. Henkes & J. L. Ingen), pp. 374–386. Elsevier.

Berlin, S., Lundbladh, A. & Henningson, D. S. 1994 Spatial simulations of oblique transition. *Phys. Fluids* **6**, 1949–1951.

Coles, D. 1956 The law of the wake in the turbulent boundary layer. *J. Fluid Mech.* **1**, 191–226.

Corral, R. & Jimenez, J. 1994 Direct numerical determination of the minimum bypass Reynolds number in boundary layers. *74th Fluid Dynamics Symp., Chania, Crete, Greece*, pp. 19-1–19-9.

Dong, Y. & Cumpsty, N. A. 1990 Compressor blade boundary layers, part 1: test facility and measurements with no incident wakes; part 2: measurements with incident wakes. *Trans. ASME: J. Turbomachinery* **112**, 222–240.

Dring, R. P., Joslyn, H. D., Hardin, L. W. & Wagner, J. H. 1982 Turbine rotor-stator interaction. *Trans. ASME: J. Engng Power* **104**, 729–742.

Ghosal, S. & Rogers, M. M. 1997 A numerical study of self-similarity in a turbulent plane wake using large-eddy simulation. *Phys. Fluids* **9**, 1729–1739.

Goldstein, M. E. & Wundrow, D. W. 1998 On the environmental realizability of algebraically growing disturbances and their relation to Klebanoff modes. *Theor. Comput. Fluid Dyn.* **10**, 171–186.

Grek, H. R., Kozlov, V. V. & Ramazanov, M. P. 1985 Three types of disturbances from the point source in the boundary layer. In *Laminar Turbulent Transition 2* (ed. V. V. Kozlov), pp. 267–272. Springer.

Halstead, D. E., Wisler, D. C., Okiishi, T. H., Walker, G. J., Hodson, H. P. & Shin, H. W. 1997 Boundary layer development in axial compressors and turbines – part 1: composite picture; part 2: compressors; part 3: LP turbines; part 4: computations and analysis. *Trans. ASME: J. Turbomachinery* **119**, 114–127, 128–138, 225–237, 426–443.

Hamilton, J. M., Kim, J. & Waleffe, F. 1995 Regeneration mechanisms of near-wall turbulence structures. *J. Fluid Mech.* **287**, 317–348.

Hancock, P. E. & Bradshaw, P. 1989 Turbulence structure of a boundary layer beneath a turbulent free stream. *J. Fluid Mech.* **205**, 45–76.

Henningson, D. S. & Kim, J. 1991 On turbulent spots in plane Poiseuille flow. *J. Fluid Mech.* **228**, 183–205.

Henningson, D. S., Lundbladh, A. & Johansson, A. V. 1993 A mechanism for bypass transition from localized disturbances in wall-bounded shear flows. *J. Fluid Mech.* **250**, 169–207.

Henningson, D. S., Spalart, P. R. & Kim, J. 1987 Numerical simulations of turbulent spots in plane Poiseuille and boundary layer flow. *Phys. Fluids* **30**, 2914–2917.

Hodson, H. P. 1985 Measurements of wake-generated unsteadiness in the rotor passage of axial flow turbines. *Trans. ASME: J. Engng Gas Turbine Power* **107**, 467–476.

Hodson, H. P. 1998 Blade row interactions in low pressure turbines. In *Blade Row Interference Effects in Axial Turbomachinery Stages* (ed. C. H. Sieverding & H. P. Hodson). Von Karman Institute for Fluid Dynamics Lecture Series 1998-02.

Hodson, H. P. & Dawes, W. N. 1998 On the interpretation of measured profile losses in unsteady wake-turbine blade interaction studies. *Trans. ASME: J. Turbomachinery* **120**, 276–284.

Hunt, J. C. R. & Durbin, P. A. 1999 Perturbed vortical layers and shear sheltering. *Fluid Dyn. Res.* **24**, 375–404.

Hunt, J. C. R., Durbin, P. A. & Wu, X. 1998 Interaction between free-stream turbulence and boundary layers. In *Annual Research Briefs*, pp. 113–124. Center for Turbulence Research, Stanford University,

Jacobs, R. G. & Durbin, P. A. 1998 Shear sheltering and the continuous spectrum of the Orr–Sommerfeld equation. *Phys. Fluids* **10**, 2006–2011.

Jahanmiri, M., Prabhu, A. & Narasimha, R. 1996 Experimental studies of a distorted turbulent spot in a three-dimensional flow. *J. Fluid Mech.* **329**, 1–24.

Kim, H. T., Kline, S. J. & Reynolds, W. C. 1968 An experimental study of turbulence production near a smooth wall in a turbulent boundary layer with zero pressure gradient. *Rep.* MD-20. Stanford University.

Kittichaikarn, C., Ireland, P. T., Zhong, S. & Hodson, H. P. 1999 An investigation on the onset of wake-induced transition and turbulent spot production rate using thermochromic liquid crystals. *ASME Turbo Expo '99, Indianapolis, Indiana* (submitted).

Klingmann, B. G. B. 1992 On transition due to three-dimensional disturbances in plane Poiseuille flow. *J. Fluid Mech.* **240**, 167–195.

Korakianitis, T. 1993 On the propagation of viscous wakes and potential flow in axial-turbine cascades. *Trans. ASME: J. Turbomachinery* **115**, 118–127.

Leib, S. J., Wundrow, D. W. & Goldstein, M. E. 1999 Effect of free-stream turbulence and other vortical disturbances on a laminar boundary layer. *J. Fluid Mech.* **380**, 169–203.

Liu, X. & Rodi, W. 1991 Experiments on transitional boundary layers with wake-induced unsteadiness. *J. Fluid Mech.* **231**, 229–256.

Mayle, R. E. 1991 The role of laminar turbulent transition in gas turbine engines. *Trans. ASME: J. Turbomachinery* **113**, 509–537.

Mayle, R. E. & Dullenkopf, K. 1991 More on the turbulent-strip theory for wake-induced transition. *Trans. ASME: J. Turbomachinery* **113**, 428–432.

Moser, R. D., Rogers, M. M. & Ewing, D. W. 1998 Direct simulation of a self-similar plane wake. *J. Fluid Mech.* **368**, 255–289.

Orth, U. 1993 Unsteady boundary layer transition in flow periodically disturbed by wakes. *Trans. ASME: J. Turbomachinery* **115**, 707–713.

Pfeil, H., Herbst, R. & Schroder, T. 1983 Investigation of the laminar turbulent transition of boundary layers disturbed by wakes. *Trans. ASME: J. Engng Power* **105**, 130–137.

Pierce, C. D. & Moin, P. 1998 Large eddy simulation of a confined coaxial jet with swirl and heat release. *AIAA Paper* 98-2892.

Rai, M. M. & Moin, P. 1993 Direct numerical simulation of transition and turbulence in a spatially evolving boundary layer. *J. Comput. Phys.* **109**, 169–192.

Raj, R. & Lakshminarayna, B. 1973 Characteristics of the wake behind a cascade of airfoils. *J. Fluid Mech.* **61**, 707–730.

Schlichting, H. 1979 *Boundary Layer Theory*, 7th Edn. McGraw-Hill.

Spalart, P. R. 1988 Direct simulation of a turbulent boundary layer up to $Re_\theta = 1410$. *J. Fluid Mech.* **187**, 61–98.

Spalart, P. R., Moser, R. D. & Rogers, M. M. 1991 Spectral methods for the Navier–Stokes equations with one infinite and two periodic directions. *J. Comput. Phys.* **96**, 297–324.

Walker, G. J. 1993 The role of laminar turbulent transition in gas turbine engines: a discussion. *Trans. ASME: J. Turbomachinery* **115**, 207–217.

Webster, D. R., DeGraaff, D. B. & Eaton, J. K. 1996 Turbulence characteristics of a boundary layer over a two-dimensional bump. *J. Fluid Mech.* **320**, 53–69.

Westin, K. J. A., Boiko, A. V., Klingmann, B. G. B., Kozlov, V. V. & Alfredsson, P. H. 1994 Experiments in a boundary layer subjected to free-stream turbulence. Part 1. Boundary layer structure and receptivity. *J. Fluid Mech.* **281**, 193–218.

Wu, X. & Durbin, P. A. 1998 Boundary layer transition induced by periodic wakes. *Trans. ASME: J. Turbomachinery*. (submitted).

Wu, X. & Durbin, P. A. 1999*a* Numerical simulation of heat transfer in a transitional boundary layer with passing wakes. *Trans. ASME: J. Heat Transfer* (submitted).

Wu, X. & Durbin, P. A. 1999*b* Numerical experiments and modeling of the transitional and turbulent boundary layers induced by periodically passing wakes. *Rep.* Center for Integrated Turbulence Simulation, Stanford University.

Wu, X. & Squires, K. D. 1997 Large eddy simulation of an equilibrium three-dimensional turbulent boundary layer. *AIAA J.* **35**, 67–74.

Yang, K. S., Spalart, P. R. & Ferziger, J. H. 1992 Numerical studies of natural transition in a decelerating boundary layer. *J. Fluid Mech.* **240**, 433–468.

Zhong, S., Kittichaikarn, C., Hodson, H. P. & Ireland, P. T. 1998 Visualization of turbulent spots under the influence of adverse pressure gradients. In *Proc. 8th Intl Conf. on Flow Visualization, Italy*.